

## **Alfvén : Magnetosphere -Ionosphere Connection Explorers**

Matthieu Berthomier, A. Fazakerlay, N., C. Forsyth, Raymond Pottelette,  
Olga Alexandrova, A. Anastasiadis, A. Aruliah, Pierre-Louis Blelly, Carine  
Briand, R. Bruno, et al.

► **To cite this version:**

Matthieu Berthomier, A. Fazakerlay, N., C. Forsyth, Raymond Pottelette, Olga Alexandrova, et al..  
Alfvén : Magnetosphere -Ionosphere Connection Explorers. Experimental Astronomy, springer Link,  
2011, pp.1. 10.1007/s10686-011-9273-y . hal-00656218

**HAL Id: hal-00656218**

**<https://hal.archives-ouvertes.fr/hal-00656218>**

Submitted on 16 Jul 2019

**HAL** is a multi-disciplinary open access archive for the deposit and dissemination of scientific research documents, whether they are published or not. The documents may come from teaching and research institutions in France or abroad, or from public or private research centers.

L'archive ouverte pluridisciplinaire **HAL**, est destinée au dépôt et à la diffusion de documents scientifiques de niveau recherche, publiés ou non, émanant des établissements d'enseignement et de recherche français ou étrangers, des laboratoires publics ou privés.

# Alfvén : Magnetosphere - Ionosphere Connection Explorers

M. Berthomier<sup>1</sup>, A.N. Fazakerley<sup>2</sup>, C. Forsyth<sup>2</sup>, R. Pottelette<sup>1</sup>, O. Alexandrova<sup>3</sup>, A. Anastasiadis<sup>4</sup>,  
A. Aruliah<sup>5</sup>, P.-L. Blelly<sup>6</sup>, C. Briand<sup>3</sup>, R. Bruno<sup>7</sup>, P. Canu<sup>1</sup>, B. Cecconi<sup>3</sup>, T. Chust<sup>1</sup>, I. Daglis<sup>4</sup>, J.  
Davies<sup>8</sup>, M. Dunlop<sup>8</sup>, D. Fontaine<sup>1</sup>, V. Génot<sup>6</sup>, B. Gustavsson<sup>9</sup>, G. Haerendel<sup>10</sup>, M. Hamrin<sup>11</sup>, M.  
Hapgood<sup>8</sup>, S. Hess<sup>3</sup>, D. Kataria<sup>2</sup>, K. Kauristie<sup>12</sup>, S. Kemble<sup>13</sup>, Y. Khotyaintsev<sup>14</sup>, H. Koskinen<sup>15</sup>, L.  
Lamy<sup>3</sup>, B. Lanchester<sup>9</sup>, P. Louarn<sup>6</sup>, E. Lucek<sup>16</sup>, R. Lundin<sup>17</sup>, M. Maksimovic<sup>3</sup>, J. Manninen<sup>18</sup>, A.  
Marchaudon<sup>19</sup>, O. Marghitsu<sup>20</sup>, G. Marklund<sup>21</sup>, S. Milan<sup>22</sup>, J. Moen<sup>23</sup>, F. Mottez<sup>24</sup>, H. Nilsson<sup>17</sup>, N.  
Ostgaard<sup>25</sup>, C. J. Owen<sup>2</sup>, M. Parrot<sup>19</sup>, A. Pedersen<sup>23</sup>, C. Perry<sup>8</sup>, J.-L. Pinçon<sup>19</sup>, F. Pitout<sup>26</sup>, T.  
Pulkkinen<sup>27</sup>, I. J. Rae<sup>28</sup>, L. Rezeau<sup>1</sup>, A. Roux<sup>1</sup>, I. Sandahl<sup>17</sup>, I. Sandberg<sup>4</sup>, E. Turunen<sup>29</sup>, J. Vogt<sup>30</sup>,  
A. Walsh<sup>2</sup>, C. E. J. Watt<sup>28</sup>, J. A. Wild<sup>31</sup>, M. Yamauchi<sup>17</sup>, P. Zarka<sup>3</sup>, I. Zouganelis<sup>1</sup>.

<sup>1</sup> LPP, France

<sup>2</sup> MSSL/UCL, United Kingdom

<sup>3</sup> LESIA, France

<sup>4</sup> ISARS/NOA, Greece

<sup>5</sup> UCL, United Kingdom

<sup>6</sup> IRAP, France

<sup>7</sup> IFSI, Italy

<sup>8</sup> RAL, United Kingdom

<sup>9</sup> Southampton Uni., United Kingdom

<sup>10</sup> MPE Garching, Germany

<sup>11</sup> Umeå Uni., Sweden

<sup>12</sup> FMI, Finland

<sup>13</sup> EADS Astrium, United Kingdom

<sup>14</sup> IRF-Uppsala, Sweden

<sup>15</sup> FMI/Helsinki Uni., Finland

<sup>16</sup> IC London, United Kingdom

<sup>17</sup> IRF-Kiruna, Sweden

<sup>18</sup> SGO, Finland

<sup>19</sup> LPC2E, France

<sup>20</sup> ISS, Romania

<sup>21</sup> KTH, Sweden

<sup>22</sup> Leicester Uni., United Kingdom

<sup>23</sup> Oslo Uni., Norway

<sup>24</sup> LUTH, France

<sup>25</sup> Bergen Uni., Norway

<sup>26</sup> IPAG, France

<sup>27</sup> Aalto Uni., Finland

<sup>28</sup> Alberta Uni., Canada

<sup>29</sup> EISCAT, Sweden

<sup>30</sup> Jacobs Uni. Bremen, Germany

<sup>31</sup> Lancaster Uni., United Kingdom

Corresponding Author: Prof. A.N. Fazakerley

Email [anf@mssl.ucl.ac.uk](mailto:anf@mssl.ucl.ac.uk)

Telephone: +44 1483 204 175

Fax: +44 1483 278 312

Version 3 : 31 October 2011

Revised version submitted to Experimental Astronomy

## 56 Abstract

57 The aurorae are dynamic, luminous displays that grace the night skies of Earth's high latitude  
58 regions. The solar wind emanating from the Sun is their ultimate energy source, but the chain of  
59 plasma physical processes leading to auroral displays is complex. The special conditions at the  
60 interface between the solar wind-driven magnetosphere and the ionospheric environment at the top  
61 of Earth's atmosphere play a central role. In this Auroral Acceleration Region (AAR) persistent  
62 electric fields directed along the magnetic field accelerate magnetospheric electrons to the high  
63 energies needed to excite luminosity when they hit the atmosphere. The "ideal  
64 magnetohydrodynamics" description of space plasmas which is useful in much of the  
65 magnetosphere cannot be used to understand the AAR.

66  
67 The AAR has been studied by a small number of single spacecraft missions which revealed an  
68 environment rich in wave-particle interactions, plasma turbulence, and nonlinear acceleration  
69 processes, acting on a variety of spatio-temporal scales. The pioneering 4-spacecraft Cluster  
70 magnetospheric research mission is now fortuitously visiting the AAR, but its particle instruments  
71 are too slow to allow resolve many of the key plasma physics phenomena.

72  
73 The Alfvén concept is designed specifically to take the next step in studying the aurora, by making  
74 the crucial high-time resolution, multi-scale measurements in the AAR, needed to address the key  
75 science questions of auroral plasma physics. The new knowledge that the mission will produce  
76 will find application in studies of the Sun, the processes that accelerate the solar wind and that  
77 produce aurora on other planets.

## 78 1 Introduction

79 The Alfvén mission concept proposes a new strategy for investigating universal plasma physical  
80 processes that govern what Nobel laureate Hannes Alfvén named "The Plasma Universe". Such  
81 processes encompass the acceleration of charged particles connected to the generation of  
82 electromagnetic radiation, the development of strong plasma turbulence associated with the  
83 maintenance of parallel electric fields along magnetic field lines in a collisionless plasma, and  
84 complex ion heating phenomena leading to planetary ion outflow. The most accessible regions of  
85 space for the study of these processes are the auroral regions of the Earth's magnetosphere.

86  
87 The auroral regions are a key region of our solar system: they constitute the interface that connects  
88 the distant solar wind-driven collisionless magnetosphere to the much denser ionospheric  
89 environment at the top of Earth's atmosphere. A significant fraction of the energy fed in by the  
90 solar wind to the magnetosphere is dissipated in this interface, often explosively during magnetic  
91 substorms. In this transition region, the plasma organizes itself on small spatial and fast temporal  
92 scales. The Auroral Acceleration Region (AAR) has been previously studied by a small number of  
93 single spacecraft: S3-3 (1976), DE-1 (1981), Viking (1986), Freja (1992), Polar (1995) and FAST  
94 (1996). High-time resolution FAST instruments revealed a plasma physics environment rich in  
95 wave-particle interactions, plasma turbulence, and nonlinear acceleration processes, which implied  
96 a variety of spatio-temporal scales. ESA's pioneering multi-spacecraft Cluster mission is now  
97 exploring the AAR, revealing dramatic variability of large-scale auroral phenomena. Cluster can't  
98 be used to relate these to phenomena observed by FAST as its particle instruments are too slow.

99  
100 Key science questions related to the efficiency of acceleration processes and to their ability to  
101 generate the complex features of auroral displays remain unanswered. In particular, high-time  
102 resolution observations have suggested that acceleration by Alfvén waves would be responsible for  
103 the generation of the sub-km scale auroral arcs. Single spacecraft measurements cannot evaluate  
104 the energy exchanged over a large volume of space between waves and particles. They cannot  
105 assess the efficiency of this mechanism, nor can they tell us where and when it is effective and  
106 how it relates to the evolution of the magnetosphere - ionosphere connection. From high-time  
107 resolution particle data, it has been proposed that localized parallel electric fields would explain  
108 the larger scale arcs that can be observed by onboard imagers and that are associated with large  
109 scale current structures that connect the magnetosphere to the ionosphere. Single spacecraft  
110 measurements cannot follow the formation and evolution of these transient structures or the  
111 complex transport phenomena associated with the strong plasma turbulence that develop along  
112 magnetic field lines around these structures. Fundamental questions about auroral kilometric

113 radiation, its propagation and its fine structure, and about highly variable and diverse ionospheric  
114 ion outflows, remain unanswered by earlier missions.

115

116 The Alfvén mission will be the first mission to combine high-time resolution and multi-scale  
117 measurements in the AAR. It will fly through the heart of the AAR between a few 1,000 and  
118 8,000 km altitude with two manoeuvrable spacecraft. Each spacecraft will carry the same high-  
119 time resolution instrumentation. This is essential to allow appropriate inter-spacecraft correlations  
120 and to solve the key science questions of auroral plasma physics. Thanks to the high-resolution  
121 auroral imager present on both spacecraft, this mission will offer a truly outstanding opportunity to  
122 unveil the mysteries of auroral displays. These unique capabilities together with a strong  
123 coordination with the existing network of ground based observatories provide the opportunity to  
124 improve our understanding of the magnetosphere - ionosphere connection. At the same time, the  
125 Alfvén mission will allow Europe to achieve a real breakthrough in the physics of hot collisionless  
126 plasmas. The near-Earth space plasma constitutes the most readily accessible cosmic plasma  
127 system available for extensive and detailed *in situ* observations of these physical phenomena.  
128 Dedicating this mission to Hannes Alfvén, we anticipate that it will not only tell us how our Solar  
129 System works but it will also provide a unified Cosmic Vision of our Plasma Universe.

## 130 **2 Scientific Objectives and Requirements**

### 131 **2.1 Particle acceleration by Alfvén waves and the generation of small-scale** 132 **auroral arcs**

133 Auroral particle acceleration is a key topic in magnetospheric physics. Today there is a general  
134 consensus that both quasi-static and wave electric fields contribute to field-aligned electron  
135 acceleration in the collisionless auroral plasma. However, we have yet to establish whether these  
136 acceleration mechanisms can provide sufficient energy and flux to stimulate discrete arcs over a  
137 wide range of spatio-temporal scales, and the association between each acceleration process and  
138 specific patterns of magnetosphere-ionosphere coupling is unclear.

139

140 Shear Alfvén waves are low-frequency waves that can support such accelerating parallel electric  
141 fields when their perpendicular scale lengths are small enough. Single-point observations have  
142 associated short-scale shear Alfvén waves– also called Dispersive Alfvén Waves (DAW)– with  
143 accelerated electrons [1.1]. However, there are few studies which demonstrate that electrons might  
144 gain energy at the expense of the waves during a single event due to the non-local nature of the  
145 process that develops over large distances along the magnetic field. Measurements of particle and  
146 wave energy at more than one location along the magnetic field are needed to fully characterize  
147 the acceleration by Alfvén waves in the auroral regions. For example, Dombeck et al. [1.2] had to  
148 rely upon a fortuitous conjunction between the Polar and FAST satellites, in order to correctly  
149 diagnose that the acceleration mechanism was related to DAW. Given typical number density  
150 profiles, acceleration can occur over distances of hundreds or even thousands of kilometers along  
151 the magnetic field. Consequently, systematic observations of particle and wave energy by two  
152 magnetically conjugate spacecraft are needed to fully characterize the acceleration by Alfvén  
153 waves in the auroral regions.

#### 154 *2.1.1 How efficient is Alfvénic acceleration in producing small-scale arcs?*

155 Numerical simulations indicate that Alfvénic electron acceleration can happen below 4,000 km  
156 where inertial effects dominate [e.g. 1.3], and at higher altitudes where electron pressure effects  
157 dominate [e.g. 1.4]. Depending on where and over which range of altitudes the Alfvénic  
158 acceleration takes place, this process will produce different electron energies and fluxes and  
159 auroral arcs of different widths and brightness [1.5]. Since the location of the acceleration is where  
160 the waves develop sufficiently short perpendicular scales, interferometry [e.g. 1.6] can be used to  
161 identify the perpendicular scales of the waves from electric and magnetic field measurements. This  
162 will show whether short perpendicular scales develop as the wave propagates along the field, or  
163 whether they have already developed at higher altitudes.

164

165 The Alfvén mission will supply this information by providing magnetic field conjunctions between  
166 two spacecraft in a large range of altitudes, from ~1,000 km to 8,000 km and at different latitudes  
167 and magnetic local times. The typical inter-spacecraft separation distance along the magnetic field  
168 should be of the order of 100 km to several 100's km. Observations of plasma characteristics

169 including high-time resolution 2D electron pitch-angle measurements on a few 10's ms time scale  
170 at multiple locations will be needed to identify short bursts of accelerated electrons. The ability to  
171 distinguish between DAW and small-scale magnetic field-aligned currents is also very important  
172 in the topside ionosphere [1.17]. Electromagnetic field data are necessary to diagnose the  
173 properties of DAW, to perform Poynting flux measurements, and to assess the efficiency of the  
174 Alfvénic acceleration process. By combining these data with ground-based optical data from  
175 facilities in Scandinavia and in North America, we will be able to finally understand whether  
176 Alfvén waves can feed sufficient energy into the electrons to create the small-scale (sub-km) arcs.

### 177 *2.1.2 How do Alfvén waves dissipate in auroral density inhomogeneities?*

178 Large scale density cavities (from ~10 km to a few 100's km across the magnetic field) are  
179 observed above the auroral oval. It has been suggested that Alfvén wave fronts propagating onto  
180 the edge of these cavities might distort which would lead to the formation of small perpendicular  
181 scales [1.7]. Numerical simulations have shown that the energy budget of the process delivers net  
182 electron acceleration and dissipation of the wave energy [1.8]. It is estimated that an Alfvén wave  
183 could be dissipated in a few seconds. Some aspects of this scenario have been tested using FAST  
184 observations in the topside ionosphere [1.9]. However, single spacecraft data cannot be used to  
185 analyse the full energy budget of this process. Also, the efficiency of this mechanism is highly  
186 dependent on the cavity configuration about which little is known from single spacecraft crossings.  
187

188 The Alfvén mission will establish the role of auroral density inhomogeneities in generating  
189 accelerated electrons. During the parallel phase of the mission, it will be possible to quantify the  
190 Alfvén wave energy that is dissipated in density inhomogeneities. Typical inter-spacecraft  
191 distances ranging from ~100 km to several 100's km will be needed. During the transverse phase  
192 of the mission, when the two spacecraft will cross the edges of auroral cavities at different times,  
193 we will develop a better knowledge of the temporal evolution of the density gradients. The  
194 efficiency of the process heavily depends on the cavity lifetime which will be established by  
195 systematic crossings at different altitudes, from ~1,000 km up to at least one Earth radius, and with  
196 different delays between the spacecraft, from a few to several tens of seconds.  
197

198 It will also be possible to identify cavity reformation processes: small scale secondary cavities may  
199 be excavated during DAW propagation and they might lead to subsequent dissipation and electron  
200 acceleration. Can the auroral system evolve from Alfvénic acceleration processes seen at the onset  
201 of a substorm (see next paragraph) to a quasi-static situation with particle acceleration through  
202 electrostatic structures such as strong double layers? If small-scale secondary cavities generated by  
203 dissipating DAW are a precursor of larger scale auroral cavities, then the Alfvén spacecraft will be  
204 able to observe this transition during the transverse phase of the mission.

### 205 *2.1.3 Do Alfvén waves accelerate electrons during substorm expansion phase onset?*

206 It is well known that stored energy transferred from the solar wind into near-Earth space is  
207 explosively released during substorm expansion phase onset, powering aurora and generating  
208 energetic particle populations [1.10]. The physics and the location of the region initiating the onset  
209 of the substorm expansion have remained controversial for decades [e.g., 1.11]. It is also well  
210 known that in the ionosphere, the first indication of a substorm onset is a sudden brightening of  
211 one of the quiet arcs lying near the midnight sector of the oval (or a sudden formation of an arc).  
212 However, the source of accelerated electrons that are responsible for this auroral brightening is not  
213 clear, ~50 years following its discovery.  
214

215 It has been suggested that broadband accelerated electron signatures are associated with Alfvén  
216 wave activity following substorm onset [e.g. 1.12]. Furthermore, Newell et al. [1.13] presented  
217 strong evidence that the electron energy flux from these broadband spectra increases significantly  
218 at substorm expansion phase onset. Rae et al. [1.14] demonstrate that ground-based observations  
219 of ULF wave amplitudes increase at the same time and in the same location as the first optical  
220 signatures of substorm expansion phase onset in the ionosphere. Interestingly, the onset and  
221 increase of ULF wave activity in the magnetosphere also occurs in close coincidence with the  
222 onset of ground magnetic activity [e.g., 1.15], providing a tantalising glimpse of the link between  
223 these ground-based perturbations and their possible magnetospheric counterparts. Taken together,  
224 these results suggest that ULF wave-activity, broadband aurora and substorm expansion phase  
225 onset may be intimately linked on short time scales, perhaps by the acceleration of electrons via  
226 shear Alfvén waves [e.g. 1.4].

227 The sudden formation of a parallel electric field is essential to complete substorm onset. This  
228 acceleration exhibits a two-step evolution as shown by auroral kilometric radiation observations  
229 [1.16]: the activation of low altitude acceleration (4-5000 km) which corresponds to the initial  
230 auroral brightening, and subsequent abrupt breakout of high altitude acceleration (above 6000 km)  
231 which corresponds to auroral breakup (see Figure 2.1). During the parallel phase of the mission,  
232 measurements along the same field lines at two different altitudes will show how electrons gain  
233 the energy required to power the aurora at substorm onset times. The *in situ* measurements must be  
234 made in regions of space conjugate to ground-based measurements of magnetic field and auroral  
235 imaging in order to put the measurements in the context of the global substorm evolution.

## 236 **2.2 Parallel acceleration in magnetic field-aligned current structures**

237 Among the complex current systems which connect the magnetosphere to the ionosphere, the  
238 auroral zone includes a region of quasi-stationary magnetic field-aligned currents where ion beams  
239 drift away from the ionosphere along magnetic field lines while energetic electrons travelling  
240 earthward "shower" the upper atmosphere. The associated inverted-V arcs are typically large scale  
241 and stable structures compared to those described in Section 2.1. At 3,000-4,000 km altitude,  
242 FAST satellite data have shown that a strong Double Layer (DL) localized within ten Debye  
243 lengths  $\sim 1-10$  km marks the transition from the topside ionosphere to a so-called auroral cavity  
244 where the plasma is an order of magnitude more tenuous (see Fig. 2.2). Strong DLs associated  
245 with an electric field of opposite polarity have also been shown to exist in the downward current  
246 region where electrons of ionospheric origin are accelerated upwards.

### 247 *2.2.1 How do large amplitude strongly localized parallel electric fields form and evolve?*

248 Stationary models of DL and FAST data suggest that DLs propagate along magnetic field lines at  
249 the ion-acoustic speed, which is of the order of 10 to 50 km/s in auroral regions. The amplitude of  
250 the potential step along the field-lines is inferred from 3D electric field data. However these single  
251 point measurements cannot explain how double layers form and evolve and they cannot tell us  
252 whether the lifetime of these structures can account for the quasi-stationary nature of auroral forms  
253 that are believed to be associated with them. Numerical simulations suggest that DLs form in 1D  
254 current-driven plasmas in the presence of density fluctuations [2.2]. However, they might be  
255 destabilized by their interaction with nonlinear ion structures emerging from the interaction of the  
256 accelerated ion beam with thermal plasma after  $\sim 500 \omega_{pi}^{-1}$ , which corresponds to  $\sim 1$ s in the auroral  
257 regions [2.3]. This non-stationarity would mean that parallel acceleration by a single strong DL  
258 cannot account for the quasi-stationary nature of inverted-V auroral arcs.

259  
260 During the parallel phase of the mission, we will be able to detect DLs at two different altitudes, to  
261 observe their time evolution, and to check for the stationarity of individual DLs. The time delay  
262 for observing the structure by the two spacecraft should vary from a fraction of its expected  
263 lifetime ( $\sim 1$ s) to a few times this number. Separation distances of 10 to 100 km are required to  
264 answer these questions. An auroral imager with  $< 10$  s time resolution is needed to follow the  
265 evolution of the 10-50 km scale arcs associated with quasi-stationary field-aligned currents.

### 266 *2.2.2 What is the vertical structure of Auroral Accelerating Regions (AAR)?*

267 Large scale models of the vertical structure of AAR [2.4] show that the magnetic mirror effect and  
268 the anomalous resistivity due to wave turbulence triggered by field aligned current might  
269 contribute to maintain small amplitude quasi-stationary potential drops along auroral field-lines.  
270 However numerical simulations taking into account the interaction between magnetospheric and  
271 ionospheric plasmas show how strong DLs can play a key role [2.1]. Most of the electric potential  
272 drop along the field-lines was found to be concentrated in two layers. While the low-altitude  
273 transition layer of this model would correspond to the strong DL observed by FAST, the auroral  
274 cavity would be bounded at higher altitude by a second transition layer, with a large potential drop  
275 (several kV). Can we observe this high-altitude ion transition layer? Or is there a more complex  
276 pattern of multiple transition/double layers that would simultaneously exist? Are these stationary  
277 structures? If not, is there some kind of fast reformation mechanism of the structures that would  
278 maintain a constant time-averaged accelerating potential along the auroral field-lines?

279  
280 Measurements at two altitudes will quantitatively constrain the large scale models of AAR by  
281 providing a clue on the distribution of particle distributions and electric fields. In the case of  
282 unstable layers, it will be possible to identify reformation mechanisms. We will be able to test the

283 current–voltage relationship [2.5] that plays a key role in these models. Inter-spacecraft separation  
284 distances from 50 to 500 km are required to answer these science questions. The main required  
285 measurements are dc electric field, high-time resolution electron pitch-angle, and 3D ion  
286 distributions together with auroral imager data in order to follow the evolution of the 10-50 km  
287 scale arcs that are believed to be associated with quasi-stationary magnetic field-aligned currents.

### 288 *2.2.3 What are the properties of ion hole turbulence in the upward current region?*

289 In the upward current region, above the low-altitude DL, accelerated ionospheric ions drift at  
290 different speeds due to their mass differences, whereby multi-stream plasma instabilities can  
291 develop in the auroral cavity. The FAST satellite has indeed measured ion cyclotron waves and  
292 nonlinear waves dubbed ion solitary waves [2.6]. The latter have propagation speeds in the  
293 hundreds of km/s, typically the order of the ion beams, and are characterized by a bipolar electric  
294 signal along the magnetic field with duration of 10 ms. They are usually referred to as ion holes.

295  
296 Theory and simulations have shown that ion holes can form in the cavity 50 km above its bottom.  
297 They result from the spatial growth of electrostatic waves destabilized by the two-stream  
298 instability between the beams of  $H^+$  and  $O^+$  [2.7]. They propagate with a speed on the order of 200  
299 km/s which is bracketed by that of the slow  $O^+$  beam and the faster  $H^+$  beam. From FAST  
300 measurements it was concluded that the ion holes observed had a speed larger than the  $H^+$  beam.  
301 However only the electric field intensity and the time the structure takes to transit by the satellite  
302 was directly measured. Its amplitude was indirectly estimated by evaluating the response of the  
303 electron spectrum. From this estimate, the size and finally the speed of the structure was obtained.  
304 Dual satellite measurements will provide a direct measure of the speed of ion holes by estimating  
305 the delay of the electric field signature between the spacecraft. Spacecraft distances from 10 to 100  
306 km are needed, corresponding to time delays  $<1$  s over which ion holes are expected to be stable.

307  
308 It is also known that  $O^+$  ions have a larger pitch-angle than  $H^+$  ions in these regions. This is either  
309 due to the non-adiabatic motion of  $O^+$  ions that cross the low-altitude DL or by the selective  
310 perpendicular heating of low charge/mass ratio ions by ion-cyclotron turbulence. During the  
311 parallel phase, we will be able to discriminate between the two models, since one mechanism  
312 occurs at the transition layer itself while the other occurs 50-100 km above. A spacecraft  
313 separation distance less than 200 km is needed in order to simultaneously monitor the transition  
314 layer and the region where ion holes and ion cyclotron turbulence develop. To address this topic, it  
315 is necessary to measure dc electric field and ULF/ELF waves and 3D ion distribution with mass  
316 discrimination capabilities.

### 317 *2.2.4 What are the properties of electron hole turbulence in the downward current* 318 *region?*

319 In the downward current region (Fig. 2.3), strong DLs are associated with a strong plasma  
320 turbulence composed of fast moving, large amplitude, Debye scale length, 3D electric field  
321 structures that have been interpreted as electron phase space holes [2.8]. They are generated by  
322 electron beam plasma interactions downstream of the accelerating DL. Their velocity has been  
323 estimated by interpreting their magnetic signature as due to the Lorentz transformation in the  
324 spacecraft reference frame of a purely electrostatic structure. However in weakly magnetized  
325 plasmas, recent observations by THEMIS and CLUSTER spacecraft have shown that electron  
326 holes can have a proper electromagnetic signature. Alfvén will investigate the nature (electrostatic  
327 vs. electromagnetic) of electron holes and their velocity in the strongly magnetized auroral zones.  
328 Dual spacecraft measurements will give a direct estimate of their velocity. It will then be possible  
329 to derive their spatial size and amplitude, and to check the consistency of 3D electron hole models.

330  
331 3D numerical simulations have observed the decay of 1D electron holes and the simultaneous  
332 emission of lower-hybrid waves while stability analysis of 3D electron holes suggests that a  
333 bounce resonance between trapped electrons and electrostatic whistler waves (from lower-hybrid  
334 up to plasma frequency) might take place [2.9], which would reduce electron hole lifetimes. Since  
335 electron holes have been frequently observed in association with bursts of Very Low Frequency  
336 waves [2.10], electron holes might eventually dissipate by emitting these waves (VLF saucers).  
337 During both parallel and transverse phases of the mission, the spacecraft will cross the source  
338 region of VLF saucers and at the same time they will observe the development of electron holes  
339 which will allow us to understand how this strong plasma turbulence dissipates.

## 340 **2.3 The Auroral Kilometric Radiation**

341 The very first satellites that carried radio receivers made the surprising discovery that Earth is an  
342 intense radio source implying that energy also escapes from the auroral zone. This Auroral  
343 Kilometric Radiation (AKR) extends from 50 kHz to 700 kHz. It is generated between 2,000 and  
344 12,000 km altitude with a peak power at ~5,000 km. AKR, so named because at 300 kHz it has a 1  
345 km wavelength in free space, is usually not detected on the ground because of shielding by the  
346 ionosphere. The total AKR peak power levels can be as high as  $10^9$  W during strong substorms,  
347 corresponding to several percent of the total substorm energy. Viking and FAST satellite  
348 observations have shown that the emissions occur slightly below the local gyrofrequency in  
349 regions of highly diluted plasma that contain earthward accelerated hot electrons (see Figure 2.4).  
350 A Cyclotron Maser Instability (CMI) [3.2] occurs when electrons gyrating around the magnetic  
351 field resonate with the background of EM waves. In the dilute auroral cavity, even weakly  
352 relativistic non-Maxwellian electrons may invert the absorption coefficient of EM waves in the  
353 plasma which radiates in concert like a maser and emits intense coherent radiation. CMI is most  
354 efficient when the distribution of electron perpendicular velocities presents a positive gradient over  
355 a significant fraction of the resonance curve [3.3]. FAST satellite data showed that parallel electric  
356 fields in cooperation with the magnetic mirror force lift the electron distribution into an excited  
357 level by generating a ring or horseshoe distribution with a strong perpendicular gradient. The  
358 radiation is emitted primarily in the Right hand polarized eXtraordinary(RX)-mode at the local  
359 relativistic electron gyrofrequency into a strictly perpendicular direction with respect to the  
360 magnetic field [3.4].

### 361 *2.3.1 How does the radiation escape?*

362 It is not understood however how the radiation escapes from the local density cavities where it is  
363 generated. The AKR source region lies within a density cavity bounded by a region containing a  
364 much denser thermal population (see Fig. 2.5). The perpendicular (to the magnetic field)  
365 dimension of the AKR source is typically ~100 km. The source region emissions are generated in  
366 the RX-mode, above the RX cutoff frequency which is an increasing function of the density and  
367 the magnetic field strength. Thus the density gradient at the edges of the cavity will reflect the  
368 radio waves, and in addition, earthward propagating emissions will also reflect due to the  
369 increasing magnetic field strength nearer the Earth.

370  
371 There are several possible windows of escape: for example, mode conversion to the R-mode which  
372 has a nearly parallel propagation with a small optical depth along the magnetic field, or  
373 alternatively, partial or total mode conversion at the dense plasma walls boundary into either the Z  
374 mode or the L-O mode. These modes have different polarization patterns. The CMI mechanism  
375 itself is expected to produce strongly elliptically polarized waves that shall consequently be  
376 observed at least within AKR sources. From outside of the cavities, AKR has been observed to  
377 display quasi-purely circular polarization [3.5] with a possible small parallel component [3.6]. The  
378 Alfvén spacecraft will measure the complete AKR polarization state. With two spacecraft at 10 to  
379 100 km separation distance and at different oblique angles relative to the static magnetic field, it  
380 will be possible to understand how mode conversion works. Poynting flux estimates will be  
381 essential to quantify the efficiency of the conversion mechanisms, to understand polarization  
382 transfers along the ray path and which information is carried by the radio waves reaching free  
383 space.

### 384 *2.3.2 What generates the AKR fine structure?*

385 The second unresolved problem is the enormous fine structuring of the radiation as illustrated in  
386 Figure 2.6. The spectral resolution of the AKR emission strongly suggests that a large part of the  
387 emission is made up of narrowband (down to less than 100 Hz) drifting structures. Often, the  
388 central frequency of the individual emissions varies in a systematic manner, sweeping either  
389 upward or downward across the spectrum. As AKR emissions take place near the electron  
390 cyclotron frequency, earthward (anti-earthward) drifts in space are reflected by upward  
391 (downward) drifts in frequency-time diagrams. Assuming a dipole magnetic field geometry, a  
392 bandwidth  $\Delta f \sim 100$  Hz corresponds to ~1 km for the radial size  $\Delta z$  of the elementary radiation  
393 structures. The speeds of the elementary radiators can be derived from the measurement of their  
394 instantaneous  $df/dt$ ; according to their bandwidth they are quite variable and range from the ion  
395 acoustic velocity to the electron thermal velocity.

396



397 The simplest assumption is to identify the emission sources with real, drifting small-scale (1 km  
398 corresponding to several Debye lengths) physical objects. It has been speculated that electron [3.7]  
399 or ion [3.8] phase-space holes associated with double layers as well as double layers themselves  
400 [3.9] might play a key role in generating different AKR fine structures: the parallel electric field  
401 they carry would locally modify the electron distribution function and would enhance the  
402 radiation. However, simultaneous measurements by two satellites crossing the AKR source region  
403 at two different altitudes are required to validate this scenario. Two satellites located a small  
404 distance apart along the same magnetic field lines (or close by) crossing an AKR source region at  
405 the same time will measure the AKR frequency structures together with the characteristics (scales  
406 and velocities) of any turbulent nonlinear structures moving along the magnetic field lines,  
407 enabling a test of the scenario.

408  
409 The possibility of a relationship between Alfvén waves and the generation of such AKR fine  
410 structure must be investigated as well. An Alfvén wave process is believed to play a role in the  
411 origin of some of the brightest short-burst Jovian radio emissions [3.10]. Fine structure in AKR  
412 emissions has also been observed at Earth in Alfvénic auroral acceleration regions between 2,500  
413 and 3,600 km [3.11]. With the two Alfvén spacecraft, it will be possible to investigate the  
414 generation of AKR short bursts by Alfvén wave accelerated electrons, with one spacecraft crossing  
415 the source region while the other is observing the escaping radiation.

### 416 **2.3.3 Towards astrophysical applications**

417 The AKR source regions are identical to the auroral particle acceleration regions, implying that  
418 AKR is the only auroral phenomenon that provides remote information about the vertical structure  
419 and dynamics of the acceleration region. For instance, AKR has been used to characterize the two  
420 step-evolution of auroral acceleration at substorm onset [1.15]. Most of the information we have  
421 about acceleration/heating processes comes from the radiation emitted by astrophysical objects  
422 over a wide range of wavelengths. The AKR from the Earth can be taken as the paradigm for other  
423 manifestations of intense radio emissions.

424  
425 The application of the CMI concept has been very efficient for explaining radiation from Jupiter  
426 and from other solar system magnetized planets [3.12]. The first crossings of the SKR source  
427 region at Saturn [3.13] display very close similarities with the terrestrial AKR counterpart, with  
428 some evidence of shell-like electron distributions. Another interesting similarity is that Saturn's  
429 SKR also exhibits a dual source character which might be linked to magnetotail reconnection and  
430 plasmoid/substorm evolution [3.14]. These results demonstrate that parallel acceleration and CMI  
431 generation processes do not only occur at Earth. Advances in studies of these phenomena at Earth  
432 will be applied in order to remotely probe the auroral regions of other magnetized planets.

433  
434 More generally, the mechanisms may be active at magnetized planets, magnetic stars, flare stars,  
435 pulsars, and active galactic nuclei or blazars [3.15]. Speculations about radiation emitted from  
436 sufficiently strongly magnetized extra-solar planets have been published [3.16]. Scaling laws have  
437 been derived from solar system planetary radio emissions that relate the emitted radio power to the  
438 power dissipated in the various corresponding flow-obstacle interactions. Extrapolating these  
439 scaling laws to the case of exoplanets, it has been suggested that hot Jupiters may produce very  
440 intense radio emissions due to either magnetospheric interaction with a strong stellar wind or to  
441 unipolar interaction between the planet and a magnetic star. Radiation of this kind, because it  
442 would be much stronger than any other radio emission, would allow not only allow detection of  
443 "radio-loud" extra-solar planets but also the inference of their magnetic field strengths and plasma  
444 properties. Because of its unique measurement capabilities, Alfvén will bring an improved  
445 understanding of AKR, which is needed if AKR is to become a reliable tool to probe astrophysical  
446 objects and, for example, to detect and/or characterize extra-solar planets.

### 447 **2.4 Ionospheric ion outflows**

448 The magnetosphere of the Earth has two plasma sources, the solar wind / magnetosheath at the  
449 outer boundary and the ionosphere at the inner boundary. The auroral ionosphere is a particularly  
450 important source of plasma during magnetic storms, when heavy ions of ionospheric origin can  
451 become dominant in large parts of the magnetosphere [see e.g. 4.1]. The final fate of ionospheric  
452 ions is dependent both on the magnetic connection between the source region and the  
453 magnetosphere and on the typical energy of escaping ions. The large-scale impact of ion outflow  
454 also strongly depends on its mass flux. Cusp outflow is most likely to escape from the

455 magnetosphere. Polar cap and polar cap boundary layer outflow is more likely to contribute to  
456 auroral dynamics and the development of auroral storms. None of these different source regions  
457 are uniform in space and time in the way they provide ionospheric material to the distant  
458 magnetosphere. Studies have shown a one-to-one relationship between poleward moving auroral  
459 forms (PMAFs) and ion upflow events in the auroral cusp, which indicates that the ion outflow  
460 phenomenon is driven by pulsed reconnection [4.2]. Ionospheric ion outflow can also induce the  
461 formation of low conductance regions which may affect the electrodynamics of the ionosphere-  
462 magnetosphere interaction. Finally ion outflow, in particular from the cusp and polar cap, is  
463 important from a planetology point of view, as this outflow may be lost from the atmosphere and  
464 thus affect atmospheric evolution on the long term [4.3].

#### 465 *2.4.1 What is the spatio-temporal variability of ion extraction mechanisms?*

466 The amount of ion outflow is critically dependent on the source altitude of the outflowing plasma.  
467 The richest source is typically the ionospheric F region, located at an altitude of typically 300-500  
468 km. It consists mostly of O<sup>+</sup>. Processes that can extract plasma from the ionospheric F region or  
469 below are most effective in locally removing O<sup>+</sup> ions. They can lead to very low ionospheric  
470 densities which, if the E region is also affected, can lead to conductance structures which will  
471 affect the auroral electrodynamics. The initial upflow of plasma from the F region can be studied  
472 by radars like the EISCAT facility but so far they only provided altitude profiles from one point  
473 [4.4].

474  
475 Two perpendicularly separated spacecraft will for the first time allow us to measure the spatial  
476 scales over which the extraction mechanisms operate, and separate this from the time scales for  
477 intermittent extraction. The initial upflow results from Joule heating in the ionosphere and from  
478 enhanced ambipolar diffusion caused by elevated electron temperatures which in turn are caused  
479 by (mainly soft) electron precipitation [4.5]. If there is no further energisation of the ions at higher  
480 altitude the ions will fall down into the ionosphere again. Even a little heating, well below what is  
481 needed to reach escape velocity, may stop the ions from returning to the ionosphere due to the  
482 effect of the mirror force. Ions may thus stay in an intermediate region until they are heated  
483 enough to overcome gravity [4.6].

484  
485 Two spacecraft separated in the perpendicular direction will allow us to study the spatial scales  
486 and persistence of such waves, as well as the drift of gravitationally bounded ions which are kept  
487 from returning to the ionosphere through the mirror force of the magnetic field. Systematic  
488 measurements by spacecraft aligned along the field-line will show if the waves are typically  
489 present over large distances along the field-line or if they only exist in narrow regions. Ions may  
490 also be trapped by downward directed field-aligned electric fields, not just gravity, or be heated in  
491 the parallel direction. Perpendicularly separated spacecraft will show how these conics evolve with  
492 time, whereas altitude separated spacecraft can show how they evolve along the field-line.

#### 493 *2.4.2 How efficient are the various ion energisation mechanisms?*

494 Throughout the outflow path the ions may be subject to heating and acceleration. In the main  
495 auroral oval direct acceleration by parallel electric fields is expected to be an important driver in  
496 the nightside and in the afternoon sector. However, wave particle interaction leading to transverse  
497 heating is expected to be the most important mechanism at low altitude and over extended altitude  
498 intervals in the dayside cusp/cleft and in the polar cap boundary layer in the nightside. Among the  
499 many energisation mechanisms depicted on Figure 4.1, Alfvén wave turbulence, that often takes  
500 the form of broadband ELF waves, has been studied by e.g. Chaston et al. [4.7]. It is a good  
501 candidate for the formation of regions of depleted plasma. However, it is also well-known that the  
502 presence of background field-aligned currents (which are themselves related to the dynamics of the  
503 aurora) affect the presence of ion cyclotron waves which can directly heat ions through a resonant  
504 process. FAST measurements show that the electron beam drives electrostatic ion cyclotron waves  
505 both in upgoing ion and upgoing electron beams [4.8]. Heating may also occur in association with  
506 density cavities, in particular lower hybrid cavities, low density regions which are filled with  
507 intense lower hybrid waves [4.9]. Another acceleration mechanism which is important at least for  
508 cusp and polar cap ion outflow is the centrifugal acceleration mechanism that has been studied  
509 with the Cluster spacecraft at high altitude [4.10]. Finally oblique field-aligned electric fields, as  
510 already described in Section 2, might also be important in regions of strong field-aligned currents.

511

512 A two spacecraft mission with varying perpendicular separation will allow us to study for the first  
513 time the structuring of both waves and particles at different spatial scales, thus allowing us to  
514 characterize and understand the turbulence that is related to ion heating. We will be able to  
515 systematically probe the scale size and lifetime of associated cavities and of field-aligned current  
516 regions. We will observe how associated electric fields and ion distribution functions evolve in  
517 and around the cavity / field-aligned currents. Altitude separated spacecraft will allow us to study  
518 the propagation of waves and turbulence along the field lines. These measurements will constrain  
519 the numerical models that integrate along magnetic field-lines the cumulative effect of specific  
520 energisation mechanisms and we will be able to assess their relative efficiency. Mass resolved  
521 measurements will be most important to distinguish between these different acceleration  
522 mechanisms since many of them are mass dependent. Such processes occur at all planets where  
523 ion outflow has been detected, but only at Earth is it likely that we will ever have the multi-point  
524 measurements appropriate to study the mechanisms leading to ion heating and outflow.

## 525 **3 Mission Profile**

### 526 **3.1 Introduction**

527 The minimum requirement in order to meet the science goals discussed here is for a well  
528 instrumented dual spacecraft mission, in which the spacecraft separation is varied along and across  
529 the magnetic field for selected length scales, covering the range of altitudes at which auroral  
530 particle acceleration occurs. During the preparation of the concept proposed to ESA, an alternative  
531 three spacecraft mission concept was also developed. The three spacecraft mission offered  
532 advantages such as the possibility of simultaneous measurements of perpendicular and parallel  
533 scales, and less severe reduction in science return in the event of instrument or even spacecraft  
534 failure. The three spacecraft mission was also more expensive and while it was not expected to  
535 exceed the mission cost cap, the team choose to propose the two spacecraft variant which is  
536 discussed in detail in this paper.

### 537 **3.2 Orbit Requirements**

#### 538 *3.2.1 Operational Orbits*

539 The scientific aims of the mission require that dual-spacecraft operations are performed over the  
540 range of altitudes and magnetic latitudes where the auroral acceleration region is located.  
541 Coverage of all magnetic local times is required, although a subset is of prime interest for studies  
542 of the substorm onset region in the pre-midnight MLT sector, and of the cusps on the dayside  
543 centred on noon MLT. For science planning purposes, we referred to a statistical study of the  
544 probability of observing accelerated auroral electrons with energy flux  $> 0.25 \text{ erg cm}^{-2} \text{ s}^{-1}$  for all  
545 IMF conditions [MP.1] and in particular an improved quality figure based on that study [MP.2].  
546 The region of maximum probability is within the ranges; ILAT  $65^{\circ}$ - $75^{\circ}$ , MLT 20-22 hrs; and a  
547 wider region of high probability is within the ranges; ILAT  $70^{\circ}$ - $80^{\circ}$ , MLT 12-18 hrs; ILAT  $65^{\circ}$ -  
548  $75^{\circ}$ , MLT 18-24 hrs.

549  
550 We present one possible orbit strategy that we have developed, with some assistance from CNES  
551 and Astrium. We note that more detailed follow-on studies might well result in a better optimised  
552 approach.

- 553
- 554 - Initial orbit: 500 km circular polar orbit. This is used for commissioning and as a parking  
555 orbit before transition to the main operational orbits, improving launch date flexibility.
- 556 - Reference Orbit 1 (RO1): 500 km x 4000 km elliptical polar orbit, (similar, but not  
557 identical to the orbit of the FAST spacecraft).
- 558 - Reference Orbit 2 (RO2): 500 km x 8000 km elliptical polar orbit.
- 559 - De-orbit phase: reduce perigee to 250 km, atmospheric drag gradually causes deorbit.
- 560

561 In Table 3.1 we summarise strawman parameters for the main science mission. For simplicity we  
562 set the spacecraft transition to RO1 to occur on the autumn equinox, at which time the orbit plane  
563 is required to lie in the noon-midnight meridian. The plane of the RO1 polar orbit is fixed in  
564 inertial space and will rotate about the Earth once per year (similar to Cluster or Double Star TC-  
565 2). The line of apsides of the RO1 orbit will rotate around within its orbit plane once in 192 days.

566 We wish to achieve magnetic conjunctions with the region of highest probability of observing  
567 accelerated auroral electrons while at apogee in northern hemisphere winter months, to favour co-  
568 operation with ground based optical observatories. We determined that to achieve this, the  
569 argument of perigee of the initial RO1 orbit should be  $192^\circ$  on 22 September. Similarly, the  
570 transition to RO2 which should ensure that conjunctions continue to occur over that region as the  
571 mission progresses, and we chose a transition date of 10 November 2022 at which point the  
572 argument of perigee (in both RO1 and RO2) is  $290^\circ$ . In Table 3.1 we summarise the mission orbits  
573 and timeline, and indicate an arbitrarily selected date to end the RO2 phase after two years.  
574

575 Figure 3.1 shows that there are 4 intervals with conjunctions in the 18-24 MLT sector in the  
576 northern hemisphere in the 2 years of the RO1 orbit. There are 2 more while in the RO2 orbit  
577 together with 2 intervals in the 12-18 MLT sector. There are also a similar number of southern  
578 hemisphere intervals which are equally useful for *in situ* measurements, but which will be less well  
579 supported by ground-based facilities. Since the period of rotation of the line of apsides is not an  
580 integer fraction of 1 year in either RO1 or RO2, the coverage pattern of the auroral oval changes as  
581 the mission proceeds, as indicated in Figure 3.1 (this is an area where further optimisation may be  
582 possible). The distribution in time and in ILAT/MLT of useful magnetic conjunctions while the  
583 spacecraft are in the AAR altitude range will be higher than shown in Figure 3.1 since the plots  
584 concentrate on the apogee intervals and ignore time when the spacecraft are elsewhere on their  
585 orbits but are also within useful ILAT/MLT regions.  
586

587 Figure 3.2 (upper panel) shows our estimates of the accumulated time spent with the spacecraft  
588 magnetic footprint in the auroral zone; the red line refers to the 12-18-24 MLT semi-oval, showing  
589 values of 1-2 hours per day in RO1 and more in RO2. The black line refers to all MLTs, i.e. the  
590 complete auroral oval, and shows roughly double the accumulated time.  
591

592 Significant additional scientific opportunities will arise by combining space measurements made  
593 by Alfvén with simultaneous conjugate observations of the aurora and of the detailed nature of the  
594 conjugate ionosphere made by ground observatories, particularly in Northern Europe and North  
595 America. Nordic infrastructure today [MP.3] includes EISCAT, Super-DARN, MIRACLE  
596 (Magnetometers, Ionospheric radars, Allsky Cameras Large Experiment), ALIS (Auroral Large  
597 Imaging System) and ASK (Auroral Structure and Kinetics). Furthermore, funding has been  
598 awarded for the planning of future capabilities in this region, specifically EISCAT\_3D and SIOS  
599 (Svalbard Integrated Arctic Earth Observing System). As an indication of how often such  
600 observations will be possible, Figure 3.2 (lower panel) shows the accumulated time spent with the  
601 spacecraft magnetic footprint above the Scandinavian MIRACLE network, which ranges between  
602 5-25 minutes in RO1 and ranges up to 50 minutes in RO2. These values were determined with 1  
603 minute resolution orbit data and magnetic mapping using the current IGRF magnetic field model,  
604 accounting for the Earth's rotation, spin axis orientation and dipole tilt. There will be additional  
605 useful conjunctions with the network of ground-based facilities in North America but we do not  
606 assess those here.  
607

608 The red and blue filled rectangles highlight the times at which the spacecraft conjunctions are in  
609 the regions of high probability of observing accelerated auroral electrons. It is clear from Figure  
610 3.2 that these coincide with the longer duration intervals of magnetic conjunctions with the auroral  
611 regions and intersections with the MIRACLE network, demonstrating that our mission design is  
612 reasonably effective.  
613

614 The main science goals of the mission will be addressed with both spacecraft in each of the  
615 Reference Orbits, by varying the inter-spacecraft separation in two phases; a radial (parallel)  
616 separation phase (phase A) and a transverse separation phase (phase B). In our strawman mission  
617 outline, there are 2 years in each of RO1 and RO2; further study is required to determine the most  
618 appropriate division of the time between phase A and phase B operations, but the simplest  
619 approach is to share it equally.

### 620 3.2.2 Phase A: Parallel Spacecraft Separations

621 A possible method of achieving suitable parallel separations is to modify the eccentricity of the  
622 orbit of one spacecraft without changing the semi-major axis. Differential drift of the argument of  
623 perigee produces a tilt between the lines of apsides of the orbits of the two spacecraft. The  
624 consequent radial spacecraft separation is indicated in Figure 3.3. The process can be reversed on  
625 the same spacecraft, or executed on the second (which leads to more similar fuel usage on the two

626 spacecraft) to stop the differential drift. It is more efficient to achieve the eccentricity change by  
627 decreasing perigee and raising apogee than vice versa. It is necessary to ensure that the two  
628 spacecraft are properly synchronised so that they arrive in the auroral region together, separated  
629 primarily along the magnetic field ( $\sim$  radially) without transverse separation. This can be achieved  
630 with proper planning as demonstrated by Cluster. The differential drift is relatively expensive in  
631  $\Delta v$  and fuel. For example, the drift to  $4^\circ$  tilt would take  $\sim 3$  months if using a  $\Delta v$  of 200 m/s. More  
632 fuel can achieve a given change more rapidly

### 633 **3.2.3 Phase B: Transverse Spacecraft Separations**

634 During this phase the spacecraft will be separated along the orbit track. A possible method is to  
635 temporarily alter the semi-major axis of one spacecraft, while preserving the eccentricity of its  
636 orbit. Small impulses at perigee and apogee can be used to achieve this, firstly to modify the orbit  
637 and then to return it to the original parameters. For small fuel costs (fractions of a kg,  
638 corresponding to  $\Delta v < 1$  m/s), the spacecraft separation can be varied by up to 100 km scales  
639 within 1 day. Changes can be executed more quickly for larger fuel costs. In practice, a separation  
640 scale will be selected for a set of orbits before the scale is changed to another value and the process  
641 is repeated. The along track time delay for a 10 km separation at apogee is  $\sim 2$  s, rising linearly to  
642 20 s for a 100 km gap. We note that operations at comparable small separations have already been  
643 achieved during the ESA-NASA Cluster mission and will soon be demonstrated in the NASA  
644 Magnetospheric Multi-scale Mission.

## 645 **3.3 Launcher and Spacecraft Manoeuvring Requirements**

### 646 **3.3.1 Launch to Initial Orbit**

647 The proposed launcher is Vega. The two Alfvén spacecraft can be launched from the Guiana  
648 Space Centre into an initial  $90^\circ$  inclination polar orbit of altitude 500km. The Vega User Manual,  
649 (March 2006 version) indicates that the launch vehicle can deliver 1623 kg to this orbit. We show  
650 below that the proposed spacecraft mass including fuel and 25% margin is of order 1500 kg, and  
651 thus is well within the launch vehicle performance capability. Further orbital changes can be  
652 performed with spacecraft onboard thrusters, following the example of Cluster.

### 653 **3.3.2 Transfers to Reference Orbits**

654 The feasibility of using Vega to launch two Alfvén spacecraft, each with adequate fuel to perform  
655 the mission phases outlined above, is shown in Table 3.2. The calculation is conservative as it  
656 assumes that all fuel needed for the Phase A and B operations (“Small Scale Manoeuvres”) is  
657 retained until the end of the mission, while in practice it would be used progressively during the  
658 mission. The specific impulse figures cover a range of values which includes the 280-290 s  
659 specific impulse of Cluster 10 N thrusters in pulsed or continuous mode and the 300 s recommend  
660 by Astrium for such thrusters. The 320 s case would be for a 400 N main engine as on Cluster, but  
661 not baselined for Alfvén, included for comparison. Astrium recommended that we consider 20%  
662 of the total fuel mass to be a good estimate of propulsion system mass (tanks, thrusters, associated  
663 structure). It is clear that after including a 20% system level margin, two spacecraft can be  
664 delivered to the planned 500 x 500 km altitude initial orbit by Vega. If for some reason Vega  
665 performance is in fact lower than expected at this stage of its development, our mission profile  
666 could be correspondingly adapted by lowering the apogees of the orbits, most likely without a  
667 major impact on the science.

### 668 **3.3.3 Extended mission concepts**

669 The nominal mission lifetime described here is 4 years. Significantly longer operations may be  
670 possible based on the experience of FAST in an orbit similar to RO1 ( $> 10$  years). Extended  
671 operations in any of the scientifically preferred configurations would be valuable, in order to  
672 improve statistics and coverage of the altitude range at all MLT.

673

674 An additional mission phase which could follow the RO2 phase would involve extending the  
675 differential drift of the line of apsides to  $180^\circ$ , allowing simultaneous imaging of the northern and  
676 southern hemispheres, and collection of related *in situ* data. This would provide the first

677 opportunity to systematically study the effects of the different ionospheric illumination expected in  
678 the two hemispheres.

### 679 **3.4 Ground Segment Requirements**

680 As noted above, the line of apsides will rotate completely around the Earth, in about 6.5 months  
681 for RO1 and 11 months for RO2. In order to provide good ground station visibility while lingering  
682 near apogee, ground stations in both the northern and southern hemispheres are required. Figure  
683 3.4 shows that the daily average minimum contact time for the ESA Kiruna ground station is as  
684 low as 1 hour, which can be improved to a minimum time of 4 hours if support is also provided by  
685 the Perth ground station. It is clear that there are some individual orbits where contact time with a  
686 single ground station is very low, so the spacecraft would ideally have the capability to store data  
687 from more than one orbit between opportunities to transmit the data to a ground station.  
688 Alternatively, as proposed here it may be more cost effective to use a second ground station in the  
689 other hemisphere, to ensure that there are always contact intervals of a sufficiently long duration to  
690 transmit data from at least one orbit.

691  
692 A preliminary study has demonstrated the feasibility of meeting the planned data return  
693 requirements using these ESA ground stations (for further discussion see Section 5).

## 694 **4 Model Payload**

### 695 **4.1 Overview of all proposed payload elements**

696 Each spacecraft has an identical payload, consisting of a suite of Fields and Particles sensors  
697 together with a UV auroral imager. The payload is summarised in Table 4.1 and discussed in  
698 Section 4.3 below. For the purposes of the study, three Data Processing Units were described (for  
699 the Fields, Particles and Imager) since the resources required could be conveniently estimated  
700 based on previous work. A more detailed study may show that a combined unit could deliver the  
701 necessary functionality within a smaller resource allocation than for the three separate DPUs.  
702

703 The mass of wire/stacer booms is included in E3D. The mass of the main rigid booms (4 m) is  
704 included in MAG and HFML respectively. The mass of the MNLP booms is included under  
705 MLNP. These mass and power totals may be compared with the corresponding values for the  
706 highly integrated payload of the smaller FAST spacecraft, which were 65 kg and 39 W.

### 707 **4.2 Proposed payload accommodation**

708 The suggested accommodation for the “fields” equipment is shown in Figure 4.2. There are a pair  
709 of 40 m tip-to-tip electric field booms in the spin plane; a pair of 7 m tip-to-tip spin axis electric  
710 field stacer booms; two 4 m rigid booms to support the magnetometers, search coils, and loop  
711 systems. In addition, a pair of 0.7 m booms support the Langmuir needle probes; these are tilted  
712 out of the spin plane by  $\sim 30^\circ$ .

713  
714 Figure 4.3 illustrates how the plasma instruments are mounted on a main experiment platform,  
715 looking out through the curved surface of the cylindrical spacecraft. The field of view of the  
716 plasma instruments are indicated in Figure 4.3. Plasma and Imager Instruments should be aligned  
717 with the local spacecraft radius to within 15 arcseconds. Their field of view should be clear, with  
718 margin, and should not be affected by glint. The two EESA sensors should be diametrically  
719 opposite one another, so that their combined field of view is  $360^\circ$  in each case. Similarly for IESA.

### 720 **4.3 Proposed Instrument Complement**

#### 721 **4.3.1 Overview**

722 The payload of the Alfvén mission and its accommodation on the spacecraft platform is fully  
723 adapted to the study of the AAR at high-time resolution. The Electron and Ion ElectroStatic  
724 Analyzer (EESA and IESA) provide a 2D pitch-angle distribution within 40 and 100 ms,  
725 respectively (compared to 2 to 4 s on Cluster). The 3D electric fields will be measured by E3D  
726 instead of 2D electric fields on Cluster, which is essential in order to study parallel electric fields.

727 Key magnetic field measurements are fully redundant with 2 MAG sensors, also allowing  
728 correction of any residual magnetic interference from the spacecraft. MAG and MADAM  
729 observations have some overlap and will be cross-calibrated. HFML provides a 3D measure of  
730 high-frequency magnetic waves (there was no measurement of this type on Cluster), which is most  
731 important for AKR studies. CDC will for the first time partially solve the basic spatio-temporal  
732 ambiguity between small-scale (typically between 10 m and 5 km) current structures and  
733 dispersive Alfvén waves. The High Frequency Receiver (HFR) will continuously provide the  
734 complete spectral matrix of electromagnetic waves which will be a first at high frequency in the  
735 AAR and a key measurement to understand how AKR escapes from the AAR and to quantify this  
736 process.

737  
738 All instruments are at Technology Readiness Level (TRL) 5 or higher at the time of writing, with  
739 the exception of IESA which is in development and expected to reach TRL 5 by spring 2012. Most  
740 instruments have spaceflight heritage, often from multiple missions, and use technologies that are  
741 well established in Europe.

742  
743 All instruments will have a standby mode (reduced power but ready to quickly begin science  
744 measurements) and one or more (but few) science operations modes. Options for internal  
745 calibration modes or engineering modes are anticipated. Some instruments may need specific  
746 commanding when the system shifts from slow survey to fast survey to burst mode.

747  
748 All instruments will undergo appropriate ground calibration. In-flight inter-calibration of  
749 instruments will be carried out using routinely acquired datasets.

#### 750 *4.3.2 3D Electric Field:*

751 The E3D electric field experiment provides rapid measurements of 3D electric field to an accuracy  
752 of 1 mV/m on the two spin plane components and 10 mV/m on the spin axis component, up to a  
753 limit of 1 V/m. It also provides an estimate of spacecraft potential up to 50 V. The technique  
754 involves measuring the probe-spacecraft potential differences on pairs of probes on opposite sides  
755 of the spacecraft. In addition to measuring slowly varying local electric fields, electric components  
756 of electrostatic and electromagnetic waves of frequencies up to a few MHz can be measured and  
757 are received and processed by other experiments (the Low and High frequency Receivers). The 20  
758 m long spin plane wire booms are deployed from units mounted on the main experiment platform.  
759 The spin axis stacer booms are shorter (3.5 m long) in order to minimise disturbance to spacecraft  
760 attitude stability. Sensors and preamplifiers are placed at the ends of the booms.

#### 761 *4.3.3 Magnetic Field: MAG*

762 The MAG magnetic field experiment provides rapid measurements of the 3D magnetic field vector  
763 in the bandwidth DC to 64 Hz in fields as strong as 65,000 nT. Instrument accuracy is of order 0.1  
764 nT, but the practical resolution of the measurements is sized in proportion to the measured field  
765 intensity due to the digitalization of the signal. With 16 bit data words, it would be 2nT. The  
766 planned rate of science data is 16 vectors/second. The technique is the widely used fluxgate  
767 method. The instrument consists of two tri-axial fluxgate magnetic field sensors, mounted at  
768 different distances along one of the rigid booms to allow identification and correction for any  
769 unexpected magnetic interference from the spacecraft. The magnetometer alignment must be  
770 stable and known to an accuracy better than 0.1°, translating to a requirement for a rigid boom and  
771 spacecraft attitude knowledge known to better than 0.1°.

#### 772 *4.3.4 Magnetic field: MADAM*

773 Disturbances to the magnetic field in the frequency range 0.1 Hz to 25 kHz will be measured by  
774 the MADAM instrument, which also measures the magnetic field from quasi-DC to a few Hz with  
775 an auxiliary sensor. The main sensor is a magnetic field search coil which consists of tri-axial loop  
776 sensors, and the auxiliary sensor is a miniature magnetoresistive sensor which is incorporated into  
777 the search coil mount. The magnetic field strength resolution is +/-10 nT in the flat part of the  
778 search-coil transfer function from 100 Hz to 10 kHz and 20 dB/decade higher outside the flat part,  
779 and +/-0.1nT for the auxiliary sensor. The instrument sensitivity can be expressed in terms of  
780 equivalent input magnetic noise levels as low as : <20 pT/√Hz at 1 Hz, 2 pT/√Hz at 10 Hz, 0.2  
781 pT/√Hz at 100 Hz, 0.025 pT/√Hz at 1 kHz. The instrument is designed to ensure that the  
782 maximum magnetic field at the spin frequency does not saturate the search coil output. The sensor

783 must be mounted on a rigid boom, at least 1 m from the spacecraft. Adequate separation from  
784 other boom payloads should also be provided. Supporting analog electronics may be mounted with  
785 the sensors on the boom, or at the foot of the boom.

#### 786 4.3.5 *Magnetic field: HFML*

787 Disturbances to the magnetic field in the frequency range 20 kHz to 2 MHz will be measured by  
788 the High Frequency Magnetic Loop instrument [P1], which thus complements the search coils.  
789 HFML uses 3 loops of diameter 20 cm each, and provides measurements of all three magnetic  
790 components, similar to the search coil. The instrument will measure Auroral Kilometric Radiation  
791 emissions, which have peak intensity in the 100's kHz range. Instrument bandwidth is 3 dB and  
792 sensitivity is  $0.3 \times 10^{-6}$  nT/ $\sqrt{\text{Hz}}$  at 1 MHz for a 20 cm diameter coil. The sensor and associated  
793 analog electronics must be mounted on a rigid boom at least 1m from the spacecraft to minimise  
794 spacecraft electromagnetic interference.

#### 795 4.3.6 *Electric Current Density: CDC*

796 The varying current density in the ELF frequency range can be directly measured by a Current  
797 Density Coil sensor [P2]. The sensor consists of a 15cm diameter toroidal coil with primary and  
798 secondary windings, and the measured quantity is AC current flowing through the loop. The  
799 technique is based on Ampère's Law. Taking account of spacecraft motion, this will reveal  
800 changes in current density (in a specific direction) as the spacecraft crosses field aligned current  
801 layers, even double layers, associated with auroral arcs. By comparing measurements from the 2  
802 spacecraft during the transverse phase, it will be possible to identify the proper motion of small-  
803 scale current structures. It will enable the distinction between small-scale current structures and  
804 Alfvén waves. The bandwidth is 3 dB (1 Hz – 450 Hz) and sensitivity is  $0.3 \times 10^{-6}$  A m<sup>-2</sup>/ $\sqrt{\text{Hz}}$  at  
805 10 Hz and  $1.0 \times 10^{-6}$  A m<sup>-2</sup>/ $\sqrt{\text{Hz}}$  at 1 Hz. The sensor and associated analog electronics must be  
806 mounted on a rigid boom at least 2 m from the spacecraft to minimise spacecraft electromagnetic  
807 interference.

#### 808 4.3.7 *Electromagnetic wave signal processing unit and sounder: AWI*

809 The main function of the Alfvén Wave Instrument is to digitize analog signals from the 3 fields  
810 and waves instruments HFML, E3D, and MADAM, to calculate Fourier spectra of the signals and  
811 to prepare data products that can be passed to the Fields DPU for downlink or on-board storage. It  
812 also contains an active sounder that excites plasma resonances in order to probe the absolute value  
813 of the electron plasma density. Internally, AWI is composed of three hardware modules that would  
814 share a common electronic box:

815  
816 HFR: The High Frequency Receiver will provide unique information about electromagnetic  
817 radiation in space plasmas by performing, for the first time, a complete goniopolarimetric study of  
818 Auroral Kilometric Radiation and other emissions like VLF saucers. The HFR performs duty  
819 cycled snapshot digitization of one of the electric and magnetic signals from the HFML or E3D  
820 instruments. It calculates the power spectra of 5 of the electric and magnetic signals in the  
821 frequency range between 8 kHz and 2 MHz together with their cross-spectra from which  
822 information about k-vector, polarization, and Poynting flux can be derived.

823  
824 EDEN: The electron density will be measured at high altitudes using the “relaxation sounder”,  
825 Electron DENsity, which is capable of measuring densities in the range 0.1-100 cm<sup>-3</sup>. Thus EDEN  
826 complements MNLP which measures denser plasmas, although EDEN operates at a lower rate  
827 than MNLP. The instrument consists of a transmitter which operates in partnership with the High  
828 Frequency Receiver. In “passive mode” the transmitter is inactive and the receiver picks up natural  
829 emissions in its frequency range. Operation in active mode produces plasma resonances that are  
830 detected by the receiver, from which plasma density can be determined. Transmitter activity lasts a  
831 few seconds at a time, and is employed perhaps only once every 1 minute, as it interferes with  
832 measurements from the other Fields instruments. Knowledge of the absolute electron number  
833 density is valuable for calibrating the particle instruments, cross-calibrating the magnetometer  
834 measurement (via the electron gyro-frequency), as well as for scientific studies. The method has  
835 been used in the AAR by Cluster. The transmitter frequency range will be increased for Alfvén.

836  
837 LFR: The Low Frequency Receiver provides complete information on Alfvén waves and strong  
838 double layers as well as on the wave turbulence associated with AKR and ion energisation



839 mechanisms. The LFR digitizes 6 electric probe potentials “6xV” and 3 electric field components  
840 “3xE” from E3D as well as 3 magnetic field oscillations from MADAM in the frequency range  
841 from DC up to 25 kHz. Using a downsampling scheme, it can provide continuous or duty cycled  
842 waveforms of these 12 quantities at various sampling rates (256 Hz, 25 kHz). It calculates their  
843 power and cross-spectra. Time resolution of the spectra can vary with mode.

#### 844 4.3.8 *Electron Electrostatic Analyser: EESA*

845 The pitch angle distribution of auroral region electrons is measured at the fast rate of 40 ms, for  
846 the energy range 4 eV to 32 keV using the Electron Electro-Static Analyser instrument which  
847 consists of two sensor units, each with a top hat electrostatic analyser and an electrostatic aperture  
848 deflection system at the entrance to the top hat. The sensors must be mounted on opposite sides of  
849 the spacecraft. The field of view of the combined instrument lies in the spin plane, but can be  
850 deflected through a few 10s of degrees as needed to ensure that it includes the magnetic field, so  
851 that continuous full pitch angle coverage is assured. There will be a total of 32 angular sectors  
852 giving pitch angle resolution of 11.25°. The geometric factor is based on the Cluster PEACE  
853 HEEA instrument, and at  $1.73 \times 10^{-2} \text{ cm}^2 \cdot \text{sr} \cdot \text{eV}/\text{eV}$  is a factor 3.4 larger than for the FAST EESA  
854 (a factor 0.28 of the FAST SESA spectrograph) so that the instrument will be well optimised for  
855 auroral electron fluxes, but able to collect distributions more quickly. The time to collect a full  
856 energy-pitch angle distribution with good statistics will be 40 ms (perhaps 20 ms), i.e. at least  
857 twice as quick as FAST. In order to sweep faster the accumulation step will be 1 millisecond and  
858 there will be 40 log-spaced energy steps spaced at about 1.5x the analyser FWHM  $\Delta E/E$ , 16%.

#### 859 4.3.9 *Ion Electrostatic Analyser: IESA*

860 The full 3D velocity distribution of ions is measured at the fast rate of 100 ms, for the energy  
861 range a few eV to 30 keV using two sensors comprising the Ion Electro-Static Analyser. The  
862 sensors must be mounted on opposite sides of the spacecraft. The technique involves a system of  
863 concentric toroidal plates with a wide effective aperture covering  $2\pi$  sr solid angle coverage, that  
864 guide ions to a 2D detector plane, where arrival directions are measured with  $\sim 12^\circ \times 12^\circ$  angular  
865 resolution. Energy selection is achieved using swept high voltages to provide 48 log-spaced energy  
866 channels at an energy resolution of 16%. The geometric factor of the pair of sensors is  $0.1$   
867  $\text{cm}^2 \cdot \text{sr} \cdot \text{eV}/\text{eV}$ , an order of magnitude larger than for the IESA on the FAST mission, allowing a  
868 time resolution of 100 ms with good counting statistics.

#### 869 4.3.10 *Ion Composition Analyser: ICA*

870 The full 3D velocity distribution for several key ion species is measured at a rate of twice per spin,  
871 for the energy range a few eV to 10 keV using a single sensor Ion Composition Analyser. The  
872 instrument will distinguish protons and oxygen ions even for weak fluxes, and will be able to  
873 resolve all major ion species ( $\text{H}^+$ ,  $\text{He}^+$ ,  $\text{He}^{2+}$ ,  $\text{O}^+$ ) in strong flux situations. Thus the sensor  
874 complements IESA, trading speed for simultaneous information about different ion species and  
875 finer energy resolution (10%). The instrument consists of a top hat entrance with electrostatic  
876 analyser followed by a light weight time of flight (i.e. non-magnetic) mass discrimination system  
877 which also has the advantage that the anti-coincidence system is relatively unsusceptible to false  
878 counts from penetrating radiation. The instrument is mounted on the curved face of the spacecraft,  
879 and its top hat field of view provides instantaneous  $360^\circ \times 11.25^\circ$  coverage, which is swept  
880 through  $4\pi$  sr during half a spacecraft spin. Typically the instrument would use 8 ms accumulation  
881 bins and a 32 step (sparse) energy sweep, collecting data from 16 anodes and 6 time-of-flight  
882 windows. The angular resolution is thus  $22.5^\circ$  in azimuth and  $15^\circ$  in polar (controlled by spin rate  
883 and energy sweep period). The geometric factor of the instrument is  $8 \times 10^{-3} \text{ cm}^2 \cdot \text{sr} \cdot \text{eV}/\text{eV}$ .

#### 884 4.3.11 *Multi-Needle Langmuir Probes: MNLP*

885 The electron density is measured at a rate of up to 10 kHz, over a density range of  $\sim 10^2 \text{ cm}^{-3}$  to  
886  $\sim 10^6 \text{ cm}^{-3}$ , (corresponding to altitudes below  $\sim 3000$  km) using a system of 3 needle probes on each  
887 of 2 booms, comprising the Multi-Needle Langmuir Probes [P3]. The technique relies on the  
888 principle that probe current squared ( $I_e^2$ ) plotted versus probe potential ( $V_p$ ) is a straight line, of  
889 which the growth rate is proportional with the electron density squared. The quality of the electron  
890 density measurements can be judged by checking the linearity of  $I_e^2$  versus  $V_p$ . This method is  
891 effective when the spacecraft potential is -1 to -2 V, which is expected in the relatively dense  
892 ionospheric plasma below 3,000-4,000 km altitude, but ceases to be useful in more rarefied plasma

893 where the spacecraft potential is a few V positive (as may be confirmed using the E3D  
894 instrument). The probes are operated at a constant potential and do not generate electromagnetic  
895 noise that could affect other instruments. The probes will provide reliable data as long as they are  
896 not in the spacecraft wake. The wake extends in the direction opposite to the spacecraft velocity  
897 vector and its size varies with the local Debye length that increases with altitude (of order 1 m at  
898 altitudes between 4,000 and 5,000 km). The proposed probe mounting of probes on two booms as  
899 illustrated above is intended to ensure that at least one probe triple is always outside the wake.

#### 900 **4.3.12 Wide-Field Auroral Imager: WFAI**

901 Auroral images at UV wavelengths will be collected from the band 140-180 nm which includes  
902 the molecular N<sub>2</sub> Lyman-Birge-Hopfield (LBH) emissions, using the Wide Field Auroral Imager  
903 [P4]. The images contain photometric information, allowing the measurement of auroral emission  
904 intensity as a function of location and time. The wide instantaneous field of view (tens of degrees)  
905 combined with the orbital motion of the platform, permits large swathes of the auroral emission  
906 region to be observed during each spacecraft pass. The instrument sensitivity limits are between 60  
907 Rayleigh and 20 kRayleigh. The angular resolution is ~ 15 arcminutes, hence the spatial resolution  
908 is ~2 km from a 500 km altitude apogee; 18 km from 4,000 km, and ~35 km from 8,000 km.  
909 Fields of view from each of the two planned operational orbits are illustrated in Fig 4.4.

910 The instrument is relatively small because it uses a radially-slumped micro-channel plate optical  
911 system in conjunction with a slumped photon-counting MCP detector. The optics and detector are  
912 separated by an interference filter deposited in a CaF<sub>2</sub> substrate, which simultaneously selected the  
913 UV band of interest and prevents electrons reaching the detector. In particular, the filter rejects the  
914 intense Lyman- $\alpha$  emission at 121.6 nm, permitting auroral emission to be imaged in both the dark  
915 and sunlit ionospheres. The readout anode provides high spatial resolution at high count rates and  
916 signal processing capability within the detector. Individual photons are detected and their arrival  
917 time noted to nanosecond accuracy, easily meeting the requirement for millisecond accuracy in  
918 order to allow reconstruction of an image from a spacecraft rotating with a 6 second spin period.  
919 The instrument should be mounted with the boresight perpendicular to the rotation axis, passing  
920 through the nadir once per rotation. The spacecraft accommodation should ensure no glint affects  
921 the instrument. Spacecraft attitude knowledge accurate to a few arcmins is required, and onboard  
922 timing should be accurate to 1 millisecond resolution.

#### 923 **4.3.13 Data Processing Units**

924 The Fields data processing unit deals with data collection and control for E3D, MAG, MADAM,  
925 HFML and CDC. It also hosts the LFR, HFR and EDEN equipment, and provides data processing,  
926 compression, and packetisation functions. The design is dual redundant. The particles data  
927 processing unit deals with data collection and control for EESA, IESA, ICA, and LMP. The  
928 system functionality includes power conversion for attached sensors, local data storage, data  
929 processing, compression, and packetisation functions. A dedicated DPU was envisaged to support  
930 the WFAI sensor. This has quite high resource requirements; a study of a significantly less  
931 resource intensive design is planned (a factor 4 lower in mass and power)

### 932 **4.4 On board data handling and Telemetry**

933 Table 4.2 shows the proposed telemetry rate for each instrument for each of the three data  
934 collection modes; slow survey, fast survey and burst mode. A triggered 30 s HFR super high time  
935 resolution E or B waveform snapshot requiring 300 Mbit is also planned for each orbit. The total  
936 rates are comparable to those of the FAST mission, which used a similar strategy.

937  
938 For example, using typical numbers from FAST of a 133 minute period orbit and a 40 minute  
939 auroral region crossing, we could consider 93 minutes in Slow Survey followed by the auroral  
940 region crossing of which 35 minutes was in Fast Survey and 5 minutes in Burst Mode. The  
941 accumulated data volume would be 246 Mbyte.

### 942 **4.5 Requirements on the Spacecraft: Interfaces, pointing and alignment**

943 The spacecraft spin axis should align with the spacecraft symmetry axis to within 0.5° to 95%  
944 confidence level (as Cluster). The spin axis should not nutate. The suggested spin period is 6 s  
945 however this parameter is flexible and should be reassessed in a detailed study phase. A shorter  
946 spin period would allow shorter intervals between imager observations of the Earth, but spin axis

947 control becomes more difficult due to the axial E3D booms. The spin axis direction and rotation  
948 phase knowledge requirements of  $\pm 0.25^\circ$  and  $\pm 0.20^\circ$  are proposed based on Cluster.  
949  
950 The spacecraft attitude should be maintained close to the orbital plane, and to within  $10^\circ$  of the  
951 typical local magnetic field direction in the auroral region (magnetic latitudes  $65^\circ$ - $75^\circ$ ) in order to  
952 support auroral particle measurements. It is also important that the spacecraft attitude should be  
953 controlled when the spin plane is near the Earth-Sun line to prevent the Sun entering the line of  
954 sight of the outward facing particle and imager instruments, and to avoid the E3D probes entering  
955 shadow. The spin axis should not lie with  $80^\circ$ - $100^\circ$  of the spacecraft-Sun vector.  
956  
957 No instruments require radiators or active thermal control in normal operation.

## 958 **5 System Requirements & Key Issues**

959 The Alfvén spacecraft have identical design and construction, and identical payloads. In preparing  
960 this proposal we are guided by experience with the NASA FAST spacecraft and the ESA Cluster  
961 spacecraft. The technical implementation of the FAST mission is described in detail in several  
962 papers in Space Science Reviews, Vol 98, Nos 1-2. The FAST spacecraft operated successfully in  
963 a 350 km x 4175 km  $83^\circ$  inclination orbit, very similar to our 500 km x 4000 km Reference Orbit  
964 1. Although its nominal lifetime was 1 year, its operational lifetime exceeded 10 years. Its science  
965 and payload design drivers are the same as for Alfvén, with two exceptions. Firstly, the Alfvén  
966 spacecraft will carry a wide field auroral imager. Secondly, the Alfvén spacecraft will carry  
967 sufficient fuel to alter their orbits; to vary their separation relative to one another, to modify their  
968 operational orbits and eventually to de-orbit themselves. The Cluster spacecraft flotilla have  
969 demonstrated that extensive manoeuvring, of the type we propose for Alfvén, may be done with  
970 small 10 N bipropellant thrusters. The Cluster spacecraft 400 N main engine was only used to get  
971 from GTO to the initial operational orbit. All other manoeuvres were achieved with 10 N thrusters.

### 972 **5.1 Attitude and orbit control**

973 The preferred spacecraft attitude is with the spin axis perpendicular to the velocity vector, i.e.  
974 parallel to the orbit plane normal. Ideally the spin plane is close to the local magnetic field plane at  
975 auroral latitudes, as noted in Section 4.5. The FAST mission achieved this goal by tilting the  
976 spacecraft spin axis relative to the orbit plane normal by  $\sim 3^\circ$ , towards alignment with the Earth's  
977 axis, so that the magnetic field lay within  $\sim 10^\circ$  of the spin plane. The arrangement is also  
978 compatible with the Alfvén auroral imager field of view requirement. All electric field boom tips  
979 should remain in sunlight. The other constraint on attitude is solar beta angle. FAST maintained  
980 this at  $90^\circ \pm 30^\circ$ , in order to ensure that spacecraft power and thermal constraints were respected.  
981 Depending on the design of the Alfvén spacecraft, a wider range of beta angle may be acceptable.  
982 Further study is needed to investigate how this constraint may conflict with the optimum attitude  
983 for scientific measurements, for example when the spacecraft orbit plane is perpendicular to the  
984 spacecraft-Sun line. FAST used magneto-torquers at low altitudes to achieve control of the spin  
985 axis. Attitude was sensed with a combination of a sun sensor, horizon crossing indicators and the 3  
986 axis magnetometer.

### 987 **5.2 On-board data handling and telemetry**

988 The FAST model of data collection involved "slow survey" data collected for a large fraction of  
989 the orbit during intervals of low electron flux, "fast survey" when electron fluxes exceed a  
990 threshold, and "burst" data during short intervals when specific triggers indicating passage through  
991 regions of particular interest (and even a "high speed burst for very short intervals"). FAST used a  
992 1 Gbit solid state recorder which is too small to contain 40 minutes of data collected in fast survey  
993 mode let alone burst mode, and smaller than could be downlinked in a typical contact period.  
994 Consequently the FAST team invested significant effort in onboard triggering to try to capture  
995 intervals of particular interest and managed the filling state of the recorder orbit by orbit.  
996

997 Our planned telemetry levels are similar to those of FAST, and by using a similar approach we  
998 could return them in the same way (the data volume mentioned in Section 4.4 could be  
999 downlinked in a 20-30 minute contact period at the maximum rate used by FAST). We propose a  
1000 simpler approach, taking advantage of the larger capacity mass memory now available (8 Gbit was  
1001 used on DEMETER, 32 Gbit may be realistic now) which allows us to return more complete  
1002 coverage in fast survey mode with an opportunity for a fixed fraction of each auroral crossing to

1003 be collected in burst mode. In order to return the larger data volume, either a longer contact period  
1004 would be used (FAST communications duration were apparently power limited, but we plan a  
1005 spacecraft with higher power) or else the following orbit would be used to complete the downlink  
1006 before new science data collection occurred.

### 1007 **5.3 Mission operations concept (ground segment)**

1008 The mission will be operated by ESOC, with communications being handled by the ESA ground  
1009 station network. The commanding and data recovery are envisaged as following the model of  
1010 Cluster or Double Star, in terms of spacecraft and payload control via time tagged commands, pre-  
1011 planned a few weeks ahead of execution, and regular scheduled data downlinks, ideally with  
1012 onboard data storage margin to allow a second try if a downlink is interrupted or not achieved for  
1013 some reason. Payload commanding will be prepared via a SOC in collaboration with PI teams. As  
1014 discussed in 3.4 above, the precession of the line of apsides means that ground stations will be  
1015 needed in both hemispheres. Figure 3.4 shows ground station access times determined using STK  
1016 software for the two main reference orbits, using ESA ground stations at Kiruna and Perth. This  
1017 confirms that the longest contact times in the 500 x 4,000 km orbit are of order 3,000 s (similar to  
1018 FAST) and shows how ground stations in opposite hemispheres complement one another to ensure  
1019 continuous availability of contact times of 2-3,000 seconds (30-50 mins), adequate to downlink an  
1020 orbit of data with some margin. The longer period 500 km x 8,000 km orbit offers contact times of  
1021 up to 5,500 s. ESOC will collect the data from the ground stations and to make it available to PI  
1022 teams via the SOC or MDC.

### 1023 **5.4 Estimated overall resources (mass and power)**

1024 We propose that the Alfvén spacecraft have a diameter of 2 m and a height of ~1m. These  
1025 dimensions are larger than FAST due to the need to accommodate fuel tanks and thrusters to  
1026 facilitate orbit manoeuvres and due to the need for a larger solar panel area to support the higher  
1027 planned payload average power. We also make the assumption that less highly integrated  
1028 spacecraft sub-systems may be more cost-effective for an ESA mission and we seek to provide a  
1029 greater degree of redundancy than was possible within the FAST design constraints. A stack  
1030 consisting of a pair of 2m diameter spacecraft, each ~1m high, is consistent with the Vega launch  
1031 shroud constraint.

1032  
1033 The proposed spacecraft mass breakdown is shown in Table 5.1. The estimate is based on the  
1034 FAST spacecraft where appropriate. Changes include (i) doubling the mass of subsystems which  
1035 grow in proportion to the doubled diameter, (ii) doubling the mass of the batteries, (iii) adding  
1036 10% to other sub-systems using the recommended Design Maturity Margin principle, (iv) adding  
1037 mass for fuel tanks and thrusters following the principle that their mass is 20% of the required fuel  
1038 mass (as advised by Astrium engineers). In addition there is an ESA system margin of 20%.

1039  
1040 We show in Table 5.1 that the planned beginning of life (BOL) solar array power is sufficient to  
1041 meet the demand (including ESA system margin) after 3 years, assuming a power decline at the  
1042 same rate as FAST. A slightly longer mission such as the 4 year mission we describe in section 3  
1043 would involve a further degradation of only a few W, and does not seem an unreasonable  
1044 proposition at this early stage in the mission design work. Batteries are needed to support the  
1045 spacecraft during eclipses of up to 45 minutes duration.

### 1046 **5.5 Specific environmental constraints (EMC., temperature, cleanliness)**

1047 In order to minimise spacecraft disturbances to the space plasma environment and to the  
1048 measurements, the spacecraft magnetic field and electric fields should be kept to a low level. Good  
1049 quality “magnetic cleanliness” can be achieved by making it a design requirement on the  
1050 spacecraft and payload, and by an explicit activity testing and verifying performance. Similarly, an  
1051 electrostatic cleanliness programme is required. The solar array and all other spacecraft surfaces  
1052 should be part of a single uniformly conducting surface in order to avoid localised areas of  
1053 differential surface charging with corresponding localised electric fields. An Indium Tin Oxide  
1054 coating on solar array cover glass provides the required conductivity. Other spacecraft surfaces  
1055 should have a covering of conducting MLI (multi-layer insulation) that is kept electrically  
1056 connected to the spacecraft structure. An electromagnetic cleanliness programme should ensure  
1057 that spacecraft sub-systems do not generate interference with measurements of high frequency  
1058 electric and magnetic field disturbances due to plasma waves.

1059  
1060 The “particles” and “imager” instruments use micro-channel plate detectors and high voltages, and  
1061 require a vacuum for safe operation. During spacecraft assembly and test it is necessary to provide  
1062 dry nitrogen purge for these instruments. During the initial days in orbit, time should be allowed  
1063 for out-gassing before these instruments are commissioned.

1064  
1065 Temperatures for inboard payload and spacecraft subsystems are expected to be kept within a  
1066 typical range of perhaps 5° to 30° C, with a margin of order 10° C. Outboard sensors are designed  
1067 for colder temperatures during normal operations and may need heaters to cope with eclipses.

## 1068 **5.6 Special requirements**

1069 We note that the radiation environment for this mission is relatively harsh. The Alfvén spacecraft  
1070 design should take account of this. Using SPENVIS we estimate the annual dose in Reference  
1071 Orbit 1 (500 km x 4,000 km,  $i = 90^\circ$ ) as 84/48/11 krad behind the equivalent of 3/4/5mm  
1072 aluminium. The annual dose reduces to ~ 52/24/11 krad in Reference Orbit 2 (500 km x 8,000 km,  
1073  $i = 90^\circ$ ) for 3/4/5 mm aluminium equivalent. For comparison, we understand that the Solar Orbiter  
1074 and Bepi-Colombo mission radiation doses are ~100 krad; our 4 year mission concept dose would  
1075 be similar for shielding of order 4-5 mm Aluminium. The dose behind 4mm Aluminium is  
1076 essentially the same dose tolerated by subsystems in the interior of FAST for 10 years, according  
1077 to a SPENVIS analysis of the FAST orbit. The longevity of the FAST spacecraft demonstrates the  
1078 success of the FAST design approach which could serve as a model for Alfvén.

# 1079 **6 Technology Development, Programmatics and** 1080 **Cost**

## 1081 **6.1 Technology Development requirements**

1082 No major spacecraft design challenges are foreseen, as all relevant technologies have already been  
1083 demonstrated by mission such as FAST, THEMIS, Cluster and the soon-to-be launched MMS.  
1084 Similarly, payload technology development requirements are rather minor. All the payload will be  
1085 at TRL5 by 2012 and all apart from IESA and WFAI have extensive flight heritage.

## 1086 **6.2 Overall mission cost analysis**

1087 Although detailed mission cost estimates are difficult, especially at such a preliminary stage, we  
1088 note that following ESA’s guidelines for an initial estimate, our mission concept cost falls well  
1089 inside the ESA M3 mission cost cap.

## 1090 **6.3 Mission Schedule Drivers, Risks and Alternate Strategies**

1091 There are no mission design related schedule drivers. The launch date is relatively flexible and not  
1092 tied to narrow launch windows as might be the case for example for a typical planetary mission.  
1093 Due to the low technical risk associated with the payload and the spacecraft designs, the mission  
1094 could be carried out on the timescale envisaged for the ESA M3 mission, leading to a launch as  
1095 early as late 2020.

# 1096 **7 Communication and Outreach**

1097 The aurora borealis or “northern lights” have captivated onlookers since the earliest humans  
1098 arrived in the polar regions. Cultures around the arctic circle have developed a range of myths and  
1099 folklore in order to explain the appearance of these ghostly lights in the night sky and this keen  
1100 interest in one of nature’s most spectacular natural phenomenon continues to the present day. The  
1101 aurora regularly appears in popular culture through film, television and literature while an entire  
1102 industry has developed to enable tourists to view the northern lights first-hand from cruise liners,  
1103 pleasure flights and arctic holidays.

## 1104 **8 Conclusions**

1105 The Alfvén mission concept is designed to make a major step forward in understanding the plasma  
1106 physics processes that ultimately generate the beautiful ever-changing aurora. These processes are  
1107 not well understood and their study will produce insights with applicability across a wide range of  
1108 astrophysical phenomena. A multi-spacecraft mission with sufficiently fast fields and particles  
1109 instrumentation is essential to meet this goal.

1110  
1111 The strong scientific return outlined in this paper can be achieved using a two spacecraft mission  
1112 which could be implemented quickly, costs significantly less than the ESA Medium Class mission  
1113 cost cap, does not rely on international partnerships and which does not involve technological  
1114 risks that might later drive up costs or introduce programme delays.

1115  
1116 In closing, we note that a three spacecraft mission, likely also affordable within the ESA M3 cost  
1117 cap, was also studied but is not reported here. The concept offers greater insurance against the risk  
1118 of instrument or spacecraft problems, and improved science return in some areas.

## 1119 **8 Acknowledgements**

1120 Special thanks are due to the CNES/PASO team and EADS Astrium UK for their contributions.  
1121 We thank Viktor Doychinov for his (post-proposal) UCL Masters degree project work which made  
1122 a detailed study of some Alfvén spacecraft sub-systems and confirmed the communications  
1123 concept. All participants gratefully acknowledge the various funding bodies which supported their  
1124 work.

## 1125 **9 References**

- 1126  
1127 [1.1] Chaston, C. C. et al. How important are dispersive Alfvén waves for auroral particle  
1128 acceleration?, *Geophys. Res. Lett.*, **34**, doi:10.1029/2006GL029144 (2007)  
1129 [1.2] Dombeck, J. C. et al. Alfvén waves and Poynting flux observed simultaneously by Polar and  
1130 FAST in the plasma sheet boundary layer, *J. Geophys. Res.*, **110**, doi:10.1029/2005JA011269  
1131 (2005)  
1132 [1.3] Chaston, C. C. et al. FAST observations of inertial Alfvén waves in the dayside aurora,  
1133 *Geophys. Res. Lett.*, **26**, 647-650 (1999)  
1134 [1.4] Watt, C. E. J. & Rankin, R. Electron trapping in shear Alfvén waves that power the Aurora,  
1135 *Phys. Rev. Lett.*, **102**, 045002 (2009)  
1136 [1.5] Chaston, C. C., et al. Width and brightness of auroral arcs driven by inertial Alfvén waves, *J.*  
1137 *Geophys. Res.*, **108**, doi:10.1029/2001JA007537 (2003)  
1138 [1.6] Stasiewicz, K. et al. Identification of widespread turbulence of dispersive Alfvén waves,  
1139 *Geophys. Res. Lett.*, **27**, 173-176 (2000)  
1140 [1.7] Génot, V. et al. A study of the propagation of Alfvén waves in the auroral density cavities, *J.*  
1141 *Geophys. Res.*, **104**, 22649-22656 (1999)  
1142 [1.8] Génot, V. et al. Alfvén wave interaction with inhomogeneous plasmas: acceleration and  
1143 energy cascade towards small-scales, *Ann. Geophys.*, **22**, 2081-2096 (2004)  
1144 [1.9] Chaston, C. C. et al. Ionospheric erosion by Alfvén waves, *J. Geophys. Res.*, **111**,  
1145 doi:10.1029/2005JA011367 (2006)  
1146 [1.10] Akasofu, S. The development of the auroral substorm, *Planet. Space Sci.*, **12**, 273-282  
1147 (1964)  
1148 [1.11] Lui, A. T. Y. A synthesis of magnetospheric substorm models, *J. Geophys. Res.*, **96**, 1849-  
1149 1856 (1991)  
1150 [1.12] Mende, S. et al. FAST and IMAGE-FUV observations of a substorm onset, *J. Geophys.*  
1151 *Res.*, **108**, doi:10.1029/2002JA009787 (2003)  
1152 [1.13] Newell, P. Substorm cycle dependence of various types of aurora, *J. Geophys. Res.*, **115**,  
1153 doi:10.1029/2010JA015331 (2010)  
1154 [1.14] Rae, I. J. et al. Optical characterization of the growth and spatial structure of a substorm  
1155 onset arc, *J. Geophys. Res.*, **115**, doi:10.1029/2010JA015376 (2010)  
1156 [1.15] Rae, I. J. et al. Timing and localization of ionospheric signatures associated with substorm  
1157 expansion phase onset, *J. Geophys. Res.*, **114**, doi:10.1029/2008JA013559 (2009)

1158 [1.16] Morioka, A. et al. Vertical evolution of the auroral acceleration at substorm onset, *Ann.*  
1159 *Geophys.*, **27**, 525-535 (2009)

1160 [1.17] Haerendel, G. Cosmic linear accelerator, ESA SP6285, vol. 1, **37**, 1988  
1161

1162 [2.1] Ergun, R. E. et al. Parallel electric fields in the upward current region of the aurora, *Phys. of*  
1163 *Plasmas*, **9**, 3695-3704 (2002)

1164 [2.2] Newman, D. et al. Dynamics and Instability of Electron Phase-Space Tubes, *Phys. Rev. Lett.*,  
1165 **86**, 1239-1242 (2001)

1166 [2.3] Goldman, M. et al. Phase-space holes due to electron and ion beams accelerated by a current-  
1167 driven potential ramp, *Nonlinear Proc. Geophys.*, **10**, 37-44 (2003)

1168 [2.4] Chiu, Y. T. & Schultz, M. Self-consistent particle and parallel electrostatic field distributions  
1169 in magnetospheric-ionospheric auroral region, *J. Geophys. Res.*, **83**, 629-642 (1978)

1170 [2.5] Knight, S., Parallel electric fields, *Planet. Space Sci.*, **21**, 741-750 (1973)

1171 [2.6] McFadden, J. et al., FAST observations of ion solitary waves, *J. Geophys. Res.*, **108**,  
1172 doi:10.1029/2002JA009485 (2003)

1173 [2.7] Muschietti, L. & Roth, I. Ion two-stream instabilities in the auroral acceleration zone, *J.*  
1174 *Geophys. Res.*, **113**, doi:10.1029/2007JA013005 (2008)

1175 [2.8] Muschietti, L. et al. Phase-space electron holes along magnetic field lines, *Geophys. Res.*  
1176 *Lett.*, **26**, 1093-1096 (1999)

1177 [2.9] Berthomier, M. et al. Stability of three-dimensional electron holes, *Phys. of Plasmas*, **15**,  
1178 doi:10.1063/1.3013452 (2008)

1179 [2.10] Ergun, R. E. et al. Electron phase-space holes and the VLF saucer source region, *Geophys.*  
1180 *Res. Lett.*, **28**, 3805-3808 (2001)  
1181

1182 [3.1] Ergun, R.E. et al. FAST satellite wave observations in the AKR source region, *Geophys. Res.*  
1183 *Lett.*, **25**, 2061-2064 (1998)

1184 [3.2] Wu, C. S. & Lee, L. C. Theory of the Terrestrial Kilometric Radiation, *Astrophys. J.* , **230**,  
1185 621-626 (1979)

1186 [3.3] Louarn, P. et al. Trapped electrons as the free energy source for auroral kilometric radiation,  
1187 *J. Geophys. Res.*, **95**, 5983-5993 (1990)

1188 [3.4] Ergun, R. E. et al. Electron cyclotron maser driven by charged particle acceleration from  
1189 magnetic-field aligned electric fields, *Astrophys. J.*, **538**, 456-474 (2000)

1190 [3.5] Panchenko, M. et al Estimation of linear wave polarization of the auroral kilometric  
1191 radiation, *Radio Science*, **43**, RS1006 (2008)

1192 [3.6] Louarn, P. & Le Quéau, D. Generation of the Auroral Kilometric Radiation in plasma  
1193 cavities, *Planetary and Space Science*, **44**, 199-224 (1996)

1194 [3.7] Pottelette, R. et al. Auroral plasma turbulence and the cause of AKR fine structure, *J.*  
1195 *Geophys. Res.*, **106**, 8465-8476 (2001)

1196 [3.8] Mutel, R. L. et al. Striated auroral kilometric radiation emission : a remote tracer of ion  
1197 solitary structures, *J. Geophys. Res.*, **111**, A10203 (2006)

1198 [3.9] Pottelette, R. et al. Electrostatic shock properties inferred from AKR fine structure, *Nonlin.*  
1199 *Processes Geophys.*, **10**, 87-92 (2003)

1200 [3.10] Hess, S. et al. Jovian S-burst generation by Alfvén waves, *J. Geophys. Res.*, **112**, A11212  
1201 (2007)

1202 [3.11] Su, Y. et al. Short-burst auroral radiations in Alfvénic acceleration regions: FAST  
1203 observations, *J. Geophys. Res.*, **113**, A08214 (2008)

1204 [3.12] Zarka, P. Radio and plasma waves at the outer planets, *Adv. Space Res.*, **33**, 2045-2060  
1205 (2004)

1206 [3.13] Lamy, L. et al., Properties of Saturn Kilometric Radiation measured within its source  
1207 region, *Geophys. Res. Lett.*, **37**, L12104 (2010)

1208 [3.14] Jackman, C. M., L. Lamy, M. P. Freeman, P. Zarka, B. Cecconi, W. S. Kurth, S. W. H.  
1209 Cowley, and M. K. Dougherty (2009), On the character and distribution of lower-frequency radio  
1210 emissions at Saturn and their relationship to substorm-like events, *J. Geophys. Res.*, **114**, A08211,  
1211 doi:10.1029/2008JA013997

1212 [3.15] Treumann, R. A. The electron cyclotron maser for astrophysical applications, *Astro. and*  
1213 *Astrophys. Rev.*, **13**, 229-315 (2006)

1214 [3.16] Zarka, P., Plasma interactions of exoplanets with their parent star and associated radio  
1215 emissions, *Planet. Space Sci.*, **55**, 598-617 (2007)  
1216

1217 [4.1] Kistler, L. et al., Cusp as a source for oxygen in the plasma sheet during geomagnetic storms,  
1218 *J. Geophys. Res.*, **115**, doi:10.1029/2009JA014838 (2010)

1219 [4.2] Moen, J. et al., On the relationship between ion upflow events and cusp auroral transients,  
1220 *Geophys. Res. Lett.*, **31**, doi:10.1029/2004GL020129 (2004)

1221 [4.3] Barabash, S. et al. Martian atmospheric erosion rates, *Science*, **315**, 501-503 (2007)

1222 [4.4] Nilsson, H. et al. The ionospheric signature of the cusp as seen by incoherent scatter radar, *J.*

1223 *Geophys. Res.*, **101**, 10947-10963 (1996)

1224 [4.5] Strangeway, R. J. et al. Factors controlling ionospheric outflows as observed at intermediate

1225 altitudes, *J. Geophys Res.*, **110**, doi:10.1029/2004JA010829 (2005)

1226 [4.6] André, M. et al. Ion energization mechanisms at 1700 km in the auroral region, *J. Geophys.*

1227 *Res.*, **103**, 4199-4122 (1998)

1228 [4.7] Chaston, C. C. et al. Auroral ion acceleration in dispersive Alfvén waves, *J. Geophys. Res.*,

1229 **109**, doi:10.1029/2003JA010053 (2004)

1230 [4.8] Cattell, C. et al. The association of electrostatic ion cyclotron waves, ion and electron beams

1231 and field-aligned currents: FAST observations of an auroral zone crossing near midnight,

1232 *Geophys. Res. Lett.*, **25**, 2053-2056 (1998)

1233 [4.9] Vago, J. L. et al. Transverse ion acceleration by localized lower hybrid waves in the topside

1234 ionosphere, *J. Geophys. Res.*, **97**, 16935-16957 (1992)

1235 [4.10] Nilsson, H. et al. An assessment of the role of the centrifugal acceleration mechanism in

1236 high altitude polar cap oxygen ion outflow, *Ann. Geophys.*, **26**, 145-157 (2008)

1237 [4.11] Wilson, G.R. et al. The relationship between suprathermal heavy ion outflow and auroral

1238 electron energy deposition: Polar /Ultraviolet Imager and FAST Auroral Snapshot/Time-of-Flight

1239 Energy Angle Mass Spectrometer observations, *J. Geophys. Res.*, **106**, 18981-18993 (2001)

1240

1241 [MP.1] Newell, P., K. Lyons and C. Meng, A large survey of electron acceleration events, *J.*

1242 *Geophys. Res.*, **101**, 2599 (1996)

1243 [MP.2] Paschmann, G., S. Haaland, R. Treumann (editors), Chapter 5, *Auroral Plasma Physics*,

1244 ISSI Space Science Series Vol **15**, Kluwer Academic Publishers (2003)

1245 [MP.3] I. Sandahl, Editor, *In the light of the aurora, Optical research in northernmost Europe*,

1246 TemaNord 2009:557, Nordic Council of Ministers, Copenhagen (2009)

1247

1248 [P1] Cavoit, C., Closed loop applied to magnetic measurements in the range of 0.1–50 MHz, *Rev.*

1249 *Sci. Instrum.*, **77**, 064703 (2006), DOI:10.1063/1.2214693).

1250 [P2] Krasnoselskikh, V. V., Natanzon, A. M., Reznikov, A. E., Schyokotov, A. Yu., Klimov, S. I.,

1251 Kruglyi, A. E., Woolliscroft, L. J. C., Current measurements in space plasmas and the problem of

1252 separating between spatial and temporal variations in the field of a plane electromagnetic wave,

1253 *Advances in Space Research*, Volume 11, Issue 9, p. 37-40, 1991.

1254 [P3] Bekkeng, T. A., K. S. Jacobsen, J. K. Bekkeng, A. Pedersen, T. Lindem, J-P. Lebreton and J.

1255 I. Moen, Design of a novel Multi-Needle Langmuir Probe System, *Meas. Sci. Technol.*, **21**,

1256 085903, doi: 10.1088/0957-0233/21/8/085903, 2010

1257 [P4] Bannister N.P., Bunce E.J., Cowley S.W.H., Fairbend R., Fraser G.W., Hamilton F.J.,

1258 Lapington J.S., Lees J.E., Lester M., Milan S.E., Pearson J.F., Price G.J., Willingale R., A Wide

1259 Field Auroral Imager (WFAI) for low Earth orbit missions, *Annales Geophysicae*, 2007 vol. 25

1260 pp.519.

1261

1262

1263

1264

1265

1266

1267

1268

1269

1270

1271

1272

1273

1274

1275

1276

1277

1278

1279

1280

1281

1282

1283



1284  
1285  
1286  
1287  
1288  
1289  
1290  
1291  
1292

1293

Orbit Phase	Perigee x apogee (km)	Orbit period	Line of apsides rotation period (days)	Mission phase start (d/m/y)	Phase duration (days)
Initial Orbit	500 x 500	1 h 34 m	n/a	flexible	flexible
Ref. Orbit 1	500 x 4,000	2 h 13 m	192	22/09/20	780
Ref. Orbit 2	500 x 8,000	3 h 02 m	331	10/11/22	721
De-orbiting	250 x 8,000	2 h 58 m	tbc	09/11/24	tbc

1294

1295 **Table 3.1** Summary of the strawman mission design parameters

1296

1297

1298

1299

1300

1301

1302

1303

1304

1305

1306

1307

1308

1309

1310

1311

1312

1313

1314

1315

1316

1317

1318

1319

1320

1321

1322

1323

1324

<b>Spacecraft Details</b>			
Engine Specific Impulse (s)	270	300	320
Dry Mass excluding propulsion system h/w (kg)	285	285	285
Dry Mass including propulsion system h/w (kg)	343	340	339
Fuel available for SSMs (kg)	50	50	50
Mass after LSMs, incl. SSMs fuel (kg)	393	390	389
<b>Initial orbit</b>			
Apogee altitude (km)	500	500	500
Inclination (deg)	90	90	90
Total Mass Vega can deliver to this orbit (kg)	1623	1623	1623
<b>Large Scale Maneuvers (LSMs)</b>			
Phase 1 Apogee Altitude (km)	4000	4000	4000
$\Delta V$ to Apogee (km/s)	0.7374	0.7374	0.7374
Phase 2 Apogee Altitude (km)	8000	8000	8000
$\Delta V$ to Apogee (km/s)	0.5119	0.5119	0.5119
De-orbiting Perigee Altitude (km)	250	250	250
$\Delta V$ to Perigee (km/s)	0.0531	0.0531	0.0531
<b>Fuel and propulsion</b>			
Total $\Delta V$ for LSMs (km/s)	1.3024	1.3024	1.3024
Fuel required for LSMs (kg)	236.4	223.34	216.69
Estimated propulsion system h/w [20% fuel] (kg)	57.279	54.667	53.337
<b>Mass Budget</b>			
Spacecraft Wet Mass at launch (kg)	629.4	613.34	605.69
Spacecraft Wet Mass (kg) + ESA system margin @ 20%	755.28	736	726.82
Two Spacecraft Wet Mass at launch (kg)	1510.6	1472	1453.6
Mass margin within Vega capability (kg)	112.45	150.99	169.35

1325

1326

1327

1328

1329

1330

1331

1332

1333

1334

1335

1336

1337

1338

1339

1340

1341

1342

1343

**Table 3.2** Demonstration that the spacecraft, payloads and fuel can be launched by Vega

1344  
1345  
1346  
1347  
1348  
1349  
1350  
1351  
1352  
1353  
1354  
1355  
1356  
1357  
1358  
1359  
1360  
1361  
1362  
1363  
1364

Payload Element	Abbrev.	CBE		TRL 2010
		Mass/kg	Power/W	
<b>Electric and magnetic fields; electromagnetic and electrostatic waves</b>				
Electric field: 3D	E3D	7.40	1.83	8
Magnetic field: 3D d.c.	MAG	4.23	3.00	7
Magnetic field: 3D a.c. (SC/MRM)	MADAM	1.22	1.43	5
Magnetic field: 3D HF loop	HFML	4.55	0.64	6
Current density (a.c.) loop/coil	CDC	2.01	0.40	6
Wave analysis (8kHz-2MHz)	AWI-HFR	1.50	5.00	7
Wave analysis (DC-16kHz)	AWI-LFR	0.45	3.20	5
Radio Sounder (electron density)	AWI-EDEN	0.80	2.07	8
Fields DPU	AWI-DPU	2.80	6.79	6
<b>Plasma characteristics</b>				
Electron distributions: 2D (fast)	EESA	6.90	5.40	5
Ion distributions: 3D (fast)	IESA	7.10	6.00	4
Ion distributions: 3D (mass)	ICA	1.90	6.43	7
Multi needle Langmuir probes	MNLP	4.28	3.40	6
Particles DPU	PDPU	2.20	5.80	6
<b>Auroral Imaging</b>				
Wide Field Auroral Imager (UV)	WFAI	3.56	10.51	5
Imager DPU	IDPU	1.80	6.15	5
<b>TOTALS</b>		<b>52.70</b>	<b>68.04</b>	

**Table 4.1** Summary of the proposed Alfvén payload (mass and power excluding ESA margins)

1365  
1366  
1367  
1368  
1369  
1370  
1371  
1372  
1373  
1374  
1375  
1376  
1377  
1378  
1379  
1380  
1381  
1382  
1383  
1384  
1385

Payload Data Rates	Slow Survey kbit/s	Fast Survey kbit/s	Burst kbit/s
MAG	1.54	1.54	1.54
LFR DC	3.07	3.07	3.07
LFR LF		28.67	49.15
LFR MF			3,932.16
LFR MF Spectra	4.27	102.40	
HFR spectra	3.20	6.40	6.40
CDC		32.00	32.00
EDEN	0.20	0.20	0.20
<b>Fields/Waves Subtotal</b>	<b>12.28</b>	<b>174.28</b>	<b>4,024.52</b>
EESA	2.05	20.50	512.00
IESA	1.02	24.58	360.45
ICA	5.00	48.00	48.00
MNLP	0.16	1.60	16.00
<b>Particles Subtotal</b>	<b>8.23</b>	<b>94.68</b>	<b>936.45</b>
WFAI	2.70	27.00	135.00
<b>Imager Subtotal</b>	<b>2.70</b>	<b>27.00</b>	<b>135.00</b>
<b>TOTAL</b>	<b>23.21</b>	<b>295.96</b>	<b>5,095.97</b>
FAST	50.00	500.00	8,000.00

**Table 4.2** Summary of payload data production rates for three rates of data collection

1386  
1387  
1388  
1389  
1390  
1391  
1392  
1393  
1394  
1395  
1396  
1397  
1398  
1399  
1400  
1401  
1402  
1403  
1404

Spacecraft Subsystem	Mass /kg	Spacecraft Subsystem	Power /W
Payload incl. booms	62.28		
Mission Unique Electronics	16.17	<b>Power demand</b>	
Battery/Shunt	25.00	Payload (all operating)	81.11
Solar array	70.80	Spacecraft (excl Transmitter)	50.00
ACS	10.67	RF system	28.00
RF system	5.72	<b>Subtotal</b>	<b>159.11</b>
Thermal system	3.30	ESA system margin @20%	31.82
Harness	18.20	<b>TOTAL required</b>	<b>190.93</b>
Test connector panel	0.44		
Structure	53.00		
Balance weight	10.60		
Launch adaptor	4.00	<b>Power supply</b>	
Miscellaneous	4.40	Solar array EOL	187.2
<b>Subtotal</b>	284.58	(ESA 20% margin on" BOL + 3 years")	
Tanks, thrusters, pipes (20% of fuel)	58.00		
<b>TOTAL</b>	342.58	Solar array EOL	234
ESA system margin @20%	68.52	(3 years, 10% margin = FAST actual)	
<b>GRAND TOTAL DRY MASS</b>	411.10		
Fuel	290.00		
ESA system margin @20% on fuel	58.00		
<b>GRAND TOTAL WET MASS</b>	759.10	<b>Solar array BOL required</b>	<b>260</b>

1423

1424 **Table 5.1** Summary of spacecraft subsystem mass, and of power budget. Ongoing further work  
1425 shows that some of these can be reduced, for example GaAs solar array technology would allow a  
1426 significant mass reduction in the solar array.

1427

1428

1429

1430

1431

1432

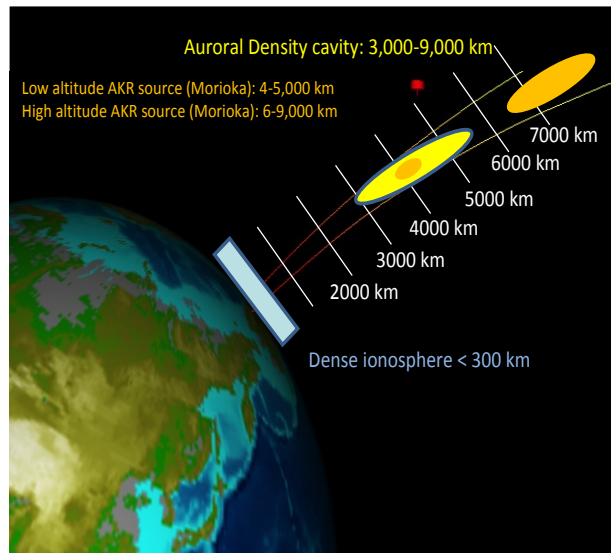
1433

1434

1435

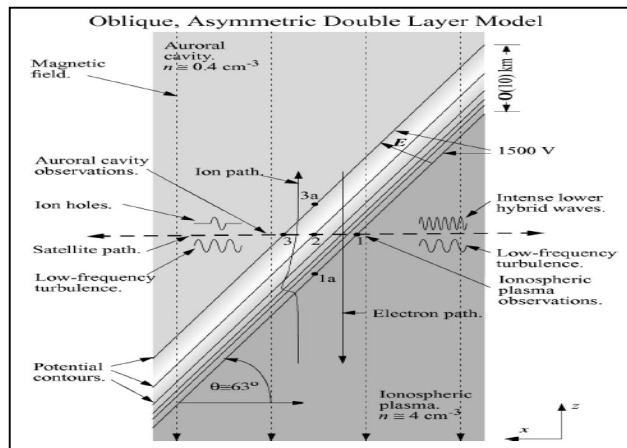
1436

1437  
1438  
1439  
1440  
1441  
1442  
1443  
1444  
1445  
1446  
1447  
1448  
1449  
1450  
1451  
1452  
1453  
1454  
1455



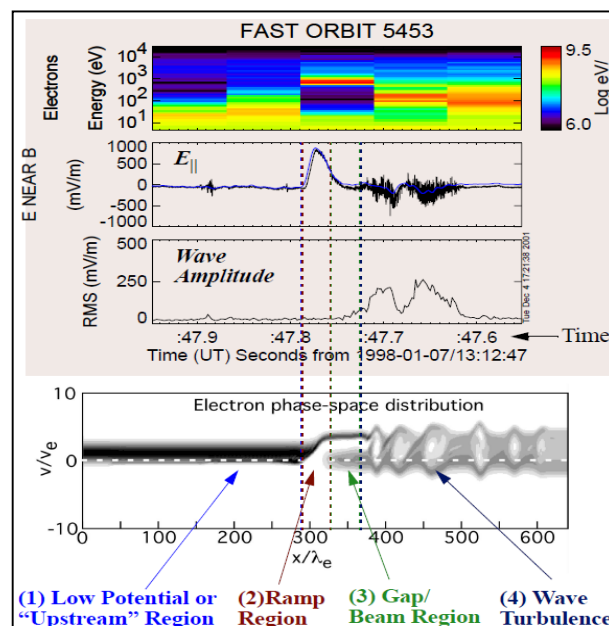
1456 **Fig. 2.1** Two-step evolution of the acceleration at substorm onset

1457  
1458  
1459  
1460  
1461  
1462  
1463  
1464  
1465  
1466  
1467  
1468  
1469  
1470  
1471  
1472

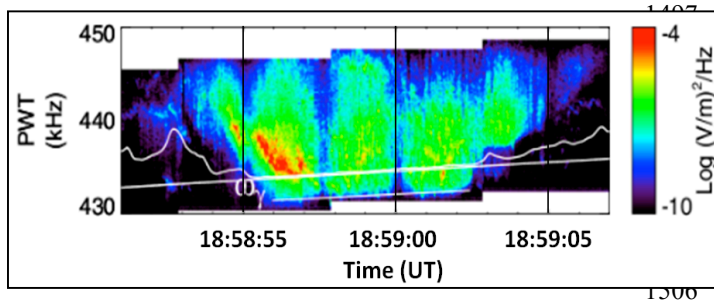


1473 **Fig. 2.2** Sketch of an oblique accelerating double layer and of its surrounding region [2.1].

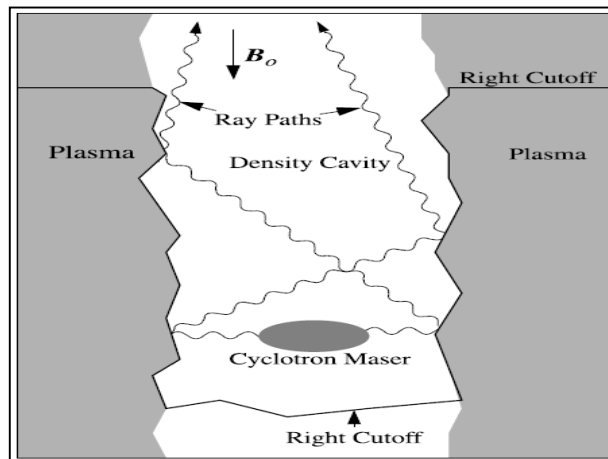
1474  
1475  
1476  
1477  
1478  
1479  
1480  
1481  
1482  
1483  
1484  
1485  
1486  
1487  
1488  
1489  
1490  
1491  
1492  
1493  
1494  
1495



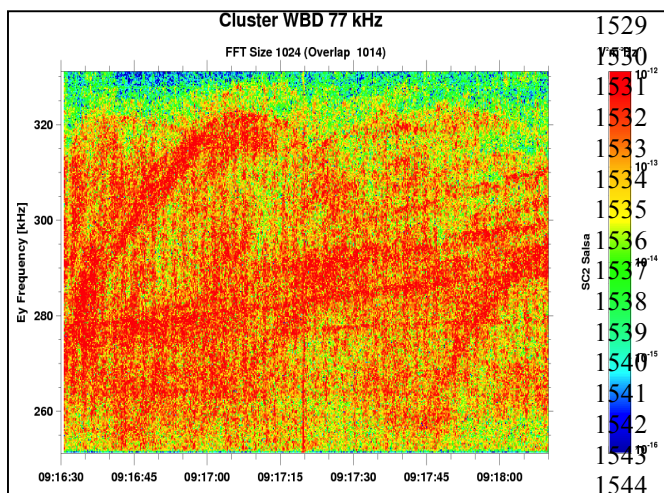
1496 **Fig. 2.3** FAST observations of DLs and wave turbulence, and numerical simulations [2.3].



1507 **Fig. 2.4** AKR FAST spectrum. The bold white line shows the electron gyrofrequency. The thin  
 1508 white line shows the expected AKR cutoff [3.1].  
 1509

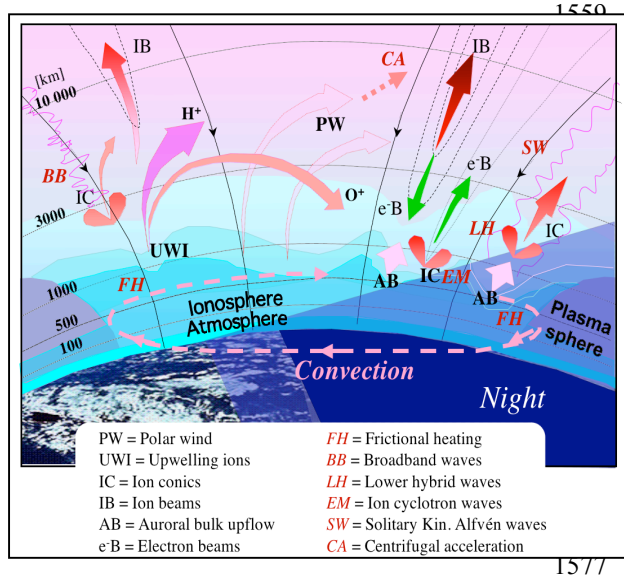


1525 **Fig. 2.5** Ray paths of AKR escaping from the auroral cavity [3.4].  
 1526  
 1527  
 1528

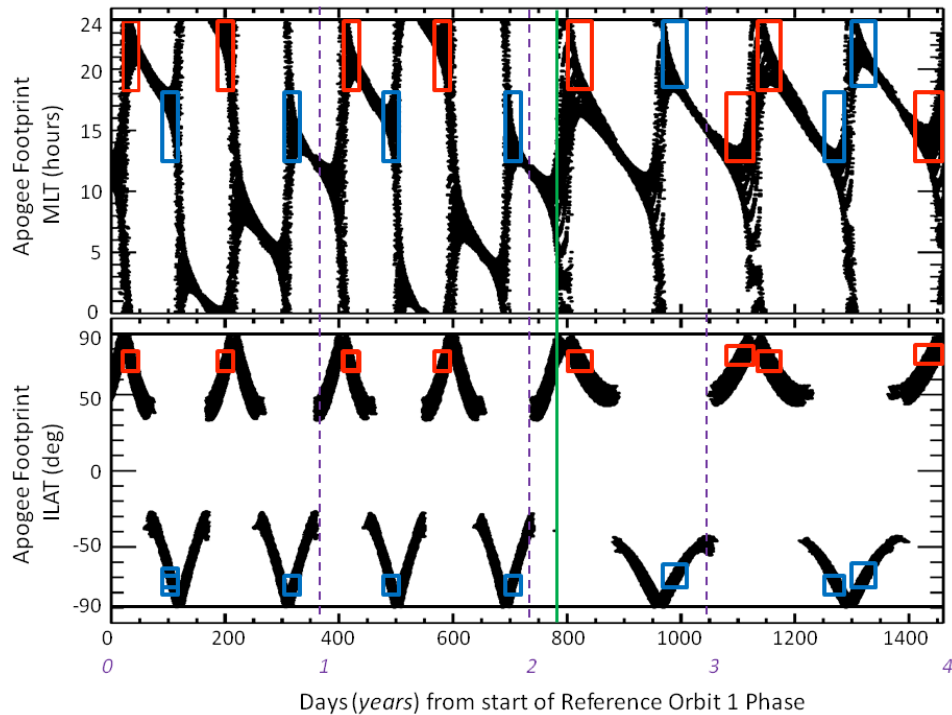


1545 **Fig. 2.6** Cluster observations of AKR fine structure (courtesy of J. Pickett).  
 1546  
 1547  
 1548  
 1549  
 1550  
 1551  
 1552  
 1553  
 1554  
 1555  
 1556

1557  
1558

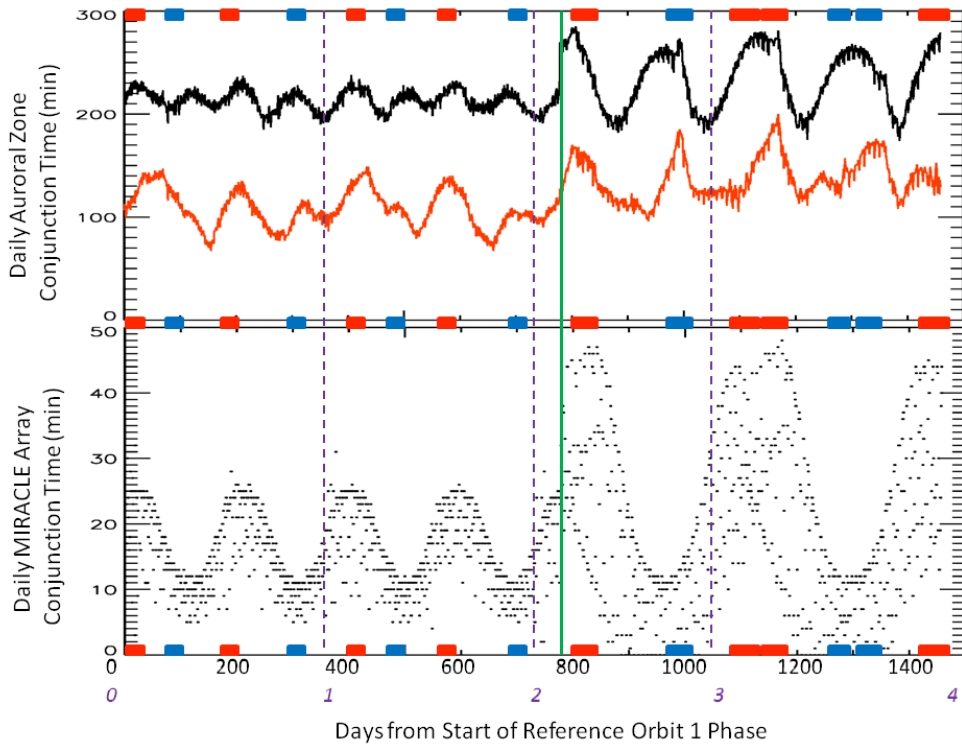


1578 **Fig. 2.7** Summary of ionospheric ion outflow related processes  
1579  
1580  
1581  
1582  
1583  
1584  
1585  
1586  
1587  
1588  
1589  
1590  
1591  
1592  
1593  
1594  
1595  
1596  
1597  
1598  
1599  
1600  
1601  
1602  
1603  
1604  
1605  
1606  
1607  
1608  
1609  
1610  
1611  
1612  
1613  
1614  
1615  
1616  
1617



1618

1619 **Fig. 3.1** Magnetic footprint coverage for times when the spacecraft are at apogee, for 4 years of  
 1620 science operations. The green line at day 720 marks the transition from Ref Orbit 1 to Ref. Orbit 2.  
 1621 Red (blue) boxes show intervals of good coverage in the northern (southern) hemisphere for the  
 1622 MLT/ILAT regions with the highest probability of seeing accelerated auroral electrons. Cusp  
 1623 observations are possible near 12 MLT at similar latitudes to those of the auroral observations.  
 1624



1625 **Fig. 3.2** Illustration of the daily accumulated time during which the spacecraft magnetic footprint  
 1626 is in the auroral zone (upper panel) or over the MIRACLE array (lower panel), for 4 years of  
 1627 science operations. As in Figure 3.1, red and blue markers show the target intervals, which in  
 1628 general coincide with longer duration conjunctions, by design.  
 1629



1630  
 1631  
 1632  
 1633  
 1634  
 1635  
 1636  
 1637  
 1638  
 1639  
 1640  
 1641  
 1642  
 1643  
 1644  
 1645  
 1646  
 1647  
 1648  
 1649  
 1650  
 1651  
 1652  
 1653

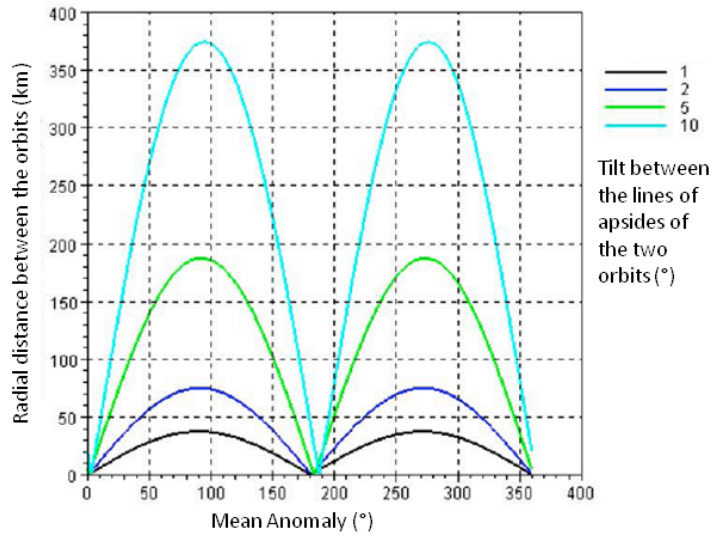
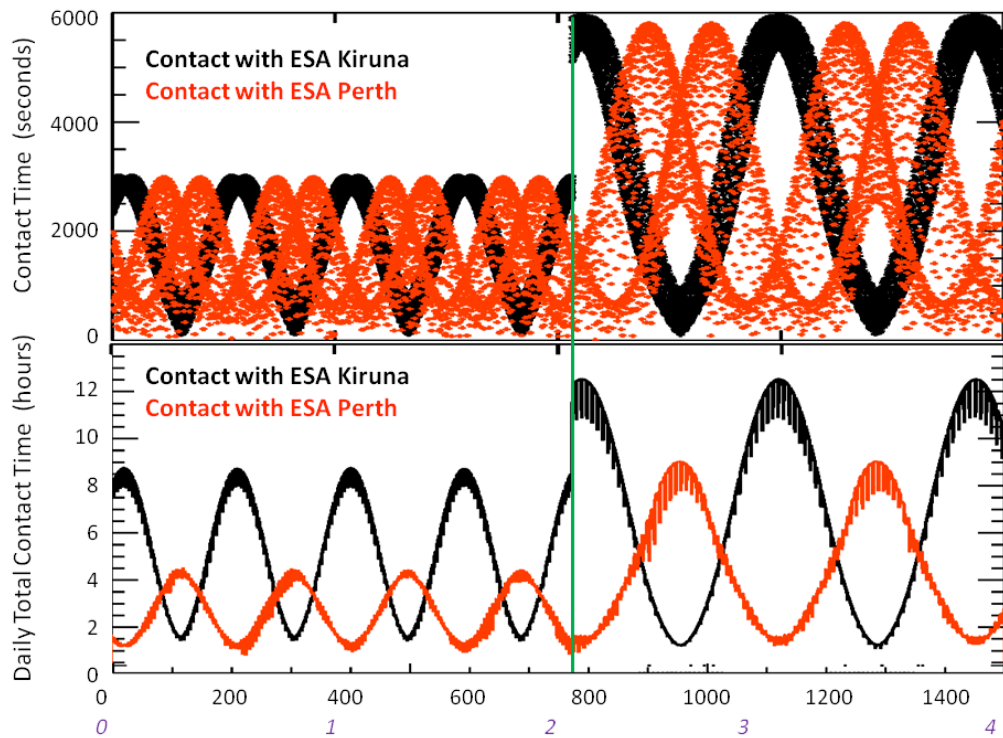
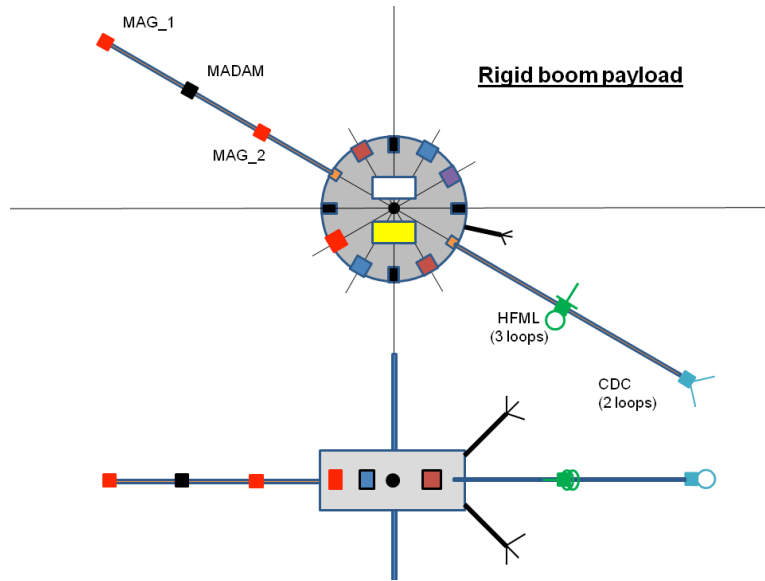


**Fig. 3.3** Illustration of the variation with mean anomaly of the radial distance between two spacecraft on otherwise identical orbits, for which the angular separation of the lines of apsides are 1,2,5 or 10°.

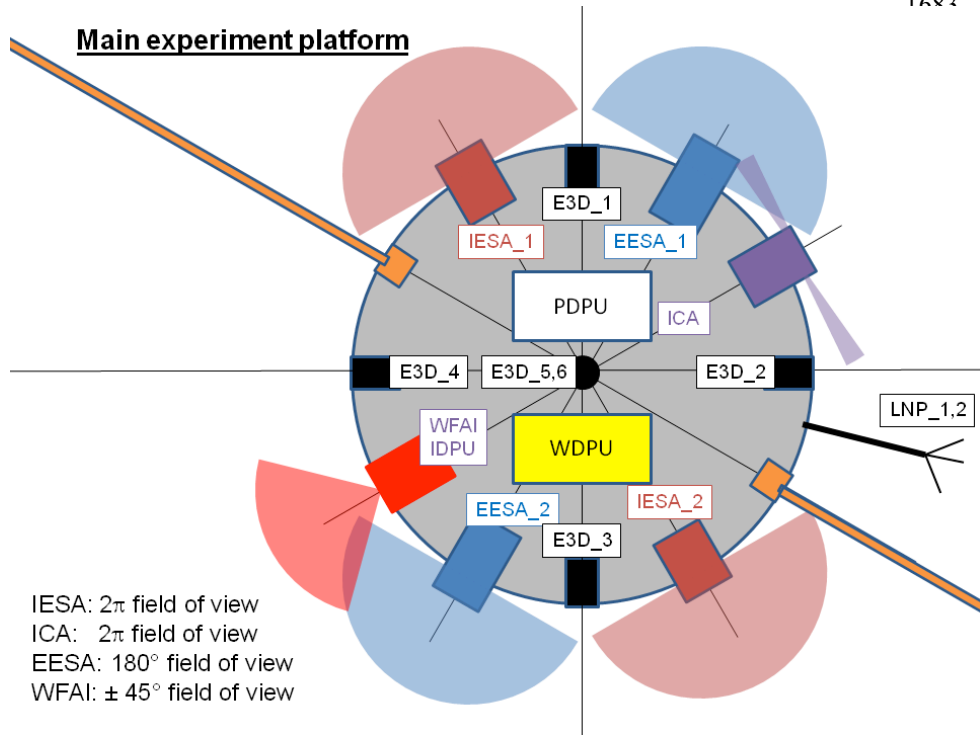


1654 **Fig. 3.4** Illustration of spacecraft-ground station access time, as the mission progresses. The upper  
 1655 panel shows the duration of contact times for each individual orbit, while the lower panel shows  
 1656 the accumulated daily total duration. Contacts with the northern hemisphere Kiruna station and the  
 1657 southern hemisphere Perth station are shown. It is clear that when one station has poor visibility of  
 1658 the spacecraft, the other can readily provide good coverage.  
 1659  
 1660  
 1661



1681 **Fig. 4.2** Plan and elevation views of the spacecraft, illustrating the various booms and the  
 1682 accommodation of the “fields” sensors

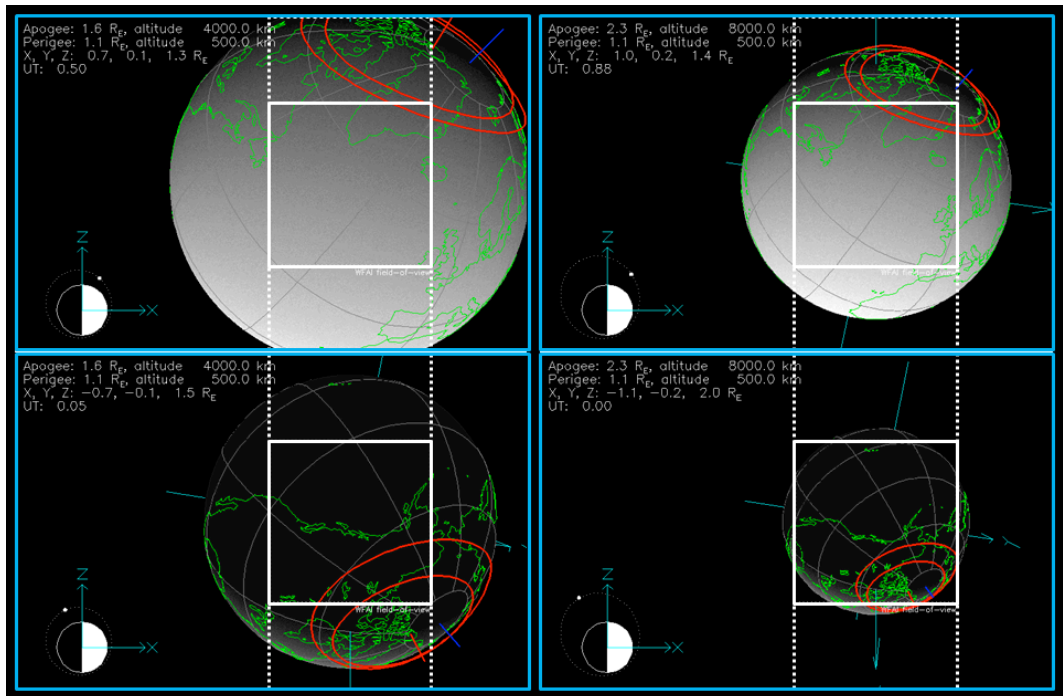
1682



1707

1708 **Fig. 4.3** Plan view of the spacecraft main experiment platform, illustrating the accommodation of  
 1709 the “particles” sensors, boom footings, auroral imager and data processing units.

1710  
 1711  
 1712  
 1713  
 1714  
 1715  
 1716  
 1717  
 1718  
 1719  
 1720  
 1721  
 1722



1723  
1724  
1725

1726 **Fig 4.4** Illustration of the instantaneous and swept fields of view of WFAI with the spacecraft  
 1727 crossing auroral magnetic field lines in the northern hemisphere, for an orbit with apogee at 60°  
 1728 northern latitude. The left/right panels show the cases of Reference Orbits 1 /2, and the day/night  
 1729 side of the Earth is shown in the top/bottom row. The solid white square is the instantaneous field  
 1730 of view when pointing to the centre of the Earth. The dotted lines show the additional coverage  
 1731 due to the rotation of WFAI with the spinning spacecraft.

1732  
1733  
1734  
1735